

LEIPZIG UNIVERSITY  
Faculty of Physics and Earth Sciences

---

## Master's Thesis

---

# Comparing Ion and Atomic Fluxes in Filtered Cathodic Arc TiAlN Deposition

**Paul Junk**

Matriculation Number: 3706642

### **Supervisors:**

- First Supervisor: Prof. Dr. Benjamin Dietzek-Ivanšić  
Leipzig University  
Director, Leibniz Institute of Surface Engineering (IOM)
- Second Supervisor: Dr. Dmitry Kalanov  
Leibniz Institute of Surface Engineering (IOM)

Leibniz Institute of Surface Engineering (IOM)  
Leipzig, Germany

January 27, 2026

## **Declaration of Independent Work**

I hereby declare that I have written this thesis independently and without any unauthorized assistance. I have used no sources or aids other than those indicated in the thesis and have marked all statements taken verbatim or in essence from other works as such.

The submitted thesis has not been the subject of any other examination procedure, either in full or in substantial parts. I have not submitted the same, a substantially similar, or any other thesis to another university as an examination paper.

---

Place, Date

---

Signature

---

## Contents

---

|          |   |           |
|----------|---|-----------|
| <b>1</b> | <b>Introduction and Literature Review</b>               | <b>7</b>  |
| 1.1      | Motivation . . . . .                                    | 7         |
| 1.2      | State of the art . . . . .                              | 8         |
| 1.3      | Objectives . . . . .                                    | 9         |
| <b>2</b> | <b>Theoretical Background</b>                           | <b>10</b> |
| 2.1      | Plasma generation and composition . . . . .             | 10        |
| 2.1.1    | Cathode spot plasma generation . . . . .                | 10        |
| 2.1.2    | Pulsed versus continuous arc operation . . . . .        | 11        |
| 2.1.3    | Plasma expansion and macroparticle filtering . . . . .  | 12        |
| 2.2      | Ion energies and flux in the substrate region . . . . . | 13        |
| 2.2.1    | Ion energies: origins and implications . . . . .        | 13        |
| 2.2.2    | Effect of distance on ion properties . . . . .          | 14        |
| 2.2.3    | Effect of external magnetic fields . . . . .            | 14        |
| 2.2.4    | Ion flux . . . . .                                      | 14        |
| 2.3      | Reactive process and nitrogen activation . . . . .      | 15        |
| 2.3.1    | Transition from metallic to reactive mode . . . . .     | 15        |
| 2.3.2    | Activated nitrogen species . . . . .                    | 15        |
| 2.4      | Plasma–surface interactions and film growth . . . . .   | 16        |
| 2.4.1    | Energetic condensation and subplantation . . . . .      | 16        |
| 2.4.2    | Structure-zone models . . . . .                         | 17        |
| 2.4.3    | TiAlN crystal structures . . . . .                      | 18        |
| <b>3</b> | <b>Experimental Methodology</b>                         | <b>20</b> |
| 3.1      | Experimental setup . . . . .                            | 20        |
| 3.1.1    | Vacuum & gas control . . . . .                          | 20        |

|          |   |           |
|----------|---|-----------|
| 3.1.2    | Power circuits and arc operation . . . . .                        | 21        |
| 3.1.3    | Diagnostic positioning and synchronization . . . . .              | 22        |
| 3.2      | Plasma diagnostics . . . . .                                      | 24        |
| 3.2.1    | Ion current probe . . . . .                                       | 24        |
| 3.2.2    | Quartz crystal microbalance . . . . .                             | 25        |
| 3.2.3    | Simultaneous ion probe and QCM measurements . . . . .             | 26        |
| 3.2.4    | Energy-resolving mass spectrometer (ERMS) . . . . .               | 27        |
| 3.3      | Thin film deposition and characterization . . . . .               | 31        |
| 3.3.1    | Profilometry . . . . .  | 31        |
| 3.3.2    | X-ray diffraction (XRD) . . . . .                                 | 32        |
| 3.3.3    | X-ray reflectivity (XRR) . . . . .                                | 33        |
| 3.3.4    | Scanning electron microscopy (SEM) . . . . .                      | 34        |
| 3.3.5    | Energy-dispersive X-ray spectroscopy (EDX) . . . . .              | 35        |
| 3.4      | Calculation of ion flux and total deposited flux . . . . .        | 36        |
| 3.4.1    | Ion flux from probe and ERMS measurements . . . . .               | 36        |
| 3.4.2    | Total deposited flux from QCM and film characterization . . . . . | 37        |
| <b>4</b> | <b>Results</b> . . . . .  | <b>38</b> |
| 4.1      | Mass deposition rate and ion current measurements . . . . .       | 38        |
| 4.1.1    | Metallic case . . . . .   | 40        |
| 4.1.2    | Measurements as a function of distance . . . . .                  | 41        |
| 4.1.3    | Measurements as a function of magnetic field . . . . .            | 41        |
| 4.1.4    | Measurements as a function of nitrogen pressure . . . . .         | 42        |
| 4.2      | Energy-resolved mass spectrometry results . . . . .               | 43        |
| 4.2.1    | Measurements as a function of distance . . . . .                  | 44        |
| 4.2.2    | Measurements as a function of pressure . . . . .                  | 45        |
| 4.3      | Thin film analysis . . . . .                                      | 46        |
| 4.3.1    | Profilometry . . . . .  | 47        |
| 4.3.2    | X-ray diffraction (XRD) . . . . .                                 | 47        |
| 4.3.3    | X-ray reflectometry (XRR) . . . . .                               | 49        |
| 4.3.4    | Energy dispersive X-ray spectroscopy (EDX) . . . . .              | 50        |
| 4.3.5    | Scanning electron microscopy (SEM) . . . . .                      | 51        |
| 4.4      | Particle flux calculations . . . . .                              | 53        |
| 4.4.1    | Calculation methods . . . . .                                     | 53        |
| 4.4.2    | Flux calculations for 14 cm distance studies . . . . .            | 53        |
| <b>5</b> | <b>Discussion and Summary</b> . . . . .                           | <b>55</b> |
| 5.1      | Film Growth and Microstructure . . . . .                          | 55        |
| 5.2      | Plasma transport and magnetic field effects . . . . .             | 56        |
| 5.3      | Reactive mode plasma chemistry . . . . .                          | 56        |

|          |  |           |
|----------|--|-----------|
| 5.3.1    | Activated nitrogen species . . . . .                   | 57        |
| 5.4      | Summary and Conclusions . . . . .                      | 58        |
| 5.5      | Outlook . . . . .                                      | 58        |
| <b>6</b> | <b>Acknowledgments</b>                                 | <b>59</b> |
| <b>A</b> | <b>Experimental Methods supplementary</b>              | <b>66</b> |
| A.1      | Longer QCM depositions . . . . .                       | 66        |
| A.2      | Holder assembly design . . . . .                       | 66        |
| A.3      | Data processing workflow . . . . .                     | 67        |
| A.3.1    | Data organization and logbook system . . . . .         | 67        |
| A.3.2    | Ion current data processing . . . . .                  | 67        |
| A.3.3    | QCM data processing . . . . .                          | 69        |
| A.3.4    | ERMS data processing . . . . .                         | 69        |
| A.4      | Uncertainty analysis . . . . .                         | 70        |
| A.4.1    | Primary measurements . . . . .                         | 71        |
| A.4.2    | Derived quantities . . . . .                           | 72        |
| A.4.3    | Uncertainties not quantified . . . . .                 | 72        |
| A.4.4    | Summary . . . . .                                      | 73        |
| A.5      | Langmuir probe bias voltage characterization . . . . . | 74        |
| A.6      | Ion current variation over different pulses . . . . .  | 75        |
| <b>B</b> | <b>Supplementary material</b>                          | <b>77</b> |
| B.1      | Data availability . . . . .                            | 78        |

## Abstract

Titanium aluminum nitride (Ti–Al–N) coatings are widely used in cutting tools and wear-resistant applications, but their industrial deposition typically requires use of external substrate, usually around 400 °C. Cathodic arc deposition offers room-temperature crystallization through energetic bombardment with multiply charged species. However, multiple process parameters are inherently coupled: external magnetic fields simultaneously increase both ion charge states (potential energy) and ion flux, while reactive gases alter plasma composition through charge-exchange collisions. This thesis investigates the TiAlN plasma to decouple the roles of ion flux, ion potential energy, and ion kinetic energy for room-temperature deposition of TiAlN as a function of magnetic field strength (0–0.25 T), nitrogen pressure (0–0.3 Pa), and spatial position (10–20 cm from the plasma source).

Three main diagnostics tools were used to separate energy effects in the plasma process: a Langmuir probe for ion current density, a quartz crystal microbalance for deposited mass, and an energy-resolving mass spectrometer for charge-state-resolved ion energy distributions. Measurements in metallic mode (vacuum) and reactive mode (nitrogen background) characterized the transition from metallic to reactive deposition and quantified the contribution of ionized versus neutral nitrogen species to film growth.

The results show that increasing the magnetic field strength can amplify ion flux by up to a factor of eight for the same distance between the source and the measurement spot. In the reactive process, the presence of nitrogen further boosts ion flux, as charge-exchange collisions reduce the number of highly ionized species and increase the proportion of singly ionized species. Ion energy distribution functions measured by energy-resolved mass spectrometry, shift toward lower ionization levels, when operating in reactive mode.

This work extends the ion energy decoupling framework established for (V,Al)N coatings to the industrially relevant TiAlN system and demonstrates that ion flux control via magnetic field strength provides a viable route to tailoring film crystallinity without the need of external substrate temperature.

# CHAPTER 1

---

## Introduction and Literature Review

---

### 1.1 Motivation

Titanium aluminum nitride ( $\text{Ti}_{1-x}\text{Al}_x\text{N}$ ) coatings are widely used, as protective coatings, particularly for cutting tools, because of their high hardness (25–35 GPa), thermal stability, and oxidation resistance [1]. These properties depend on maintaining the metastable cubic B1 crystal structure, which provides superior mechanical performance compared to the thermodynamically wurtzite phase [2]. Conventional deposition methods, such as magnetron sputtering require substantial substrate heating to achieve dense, crystalline coatings. Cathodic arc deposition offers a key advantage: highly ionized metal plasmas with intrinsic high ion energies enable room-temperature crystallization through energetic condensation [3].

The challenge is that cathodic arc processes depend on the interplay of several interdependent parameters. Ion energy has two components: kinetic energy from plasma expansion and potential energy from ionization. External magnetic fields can enhance ion charge states and ion flux, the latter increasing by up to an order of magnitude [4]. Adding reactive gases such as nitrogen introduces charge-exchange collisions that alter plasma composition [3]. Understanding how these parameters individually influence film properties remains a fundamental challenge for predictive thin film deposition.

## 1.2 State of the art

Recent studies have made progress in understanding and decoupling ion energy effects in cathodic arc deposition. Unutulmazsoy et al. showed that applying an external magnetic field at the plasma source increases ion charge states (and thus potential energy), while applying a substrate bias adjusts kinetic energy [5]. Their work on (V,Al)N films demonstrated that crystalline films can be deposited at room temperature through energetic ion bombardment. Unutulmazsoy et al. stated that “application of an external magnetic field also leads to an enhancement of the ion flux and hence the desired complete decoupling of the potential and kinetic energy effects requires further steps” [5]. In their study, the magnetic field not only modified ion charge states but also increased ion flux by up to a factor of 10, making it impossible to isolate the effect of potential energy from that of ion flux intensity.

Kalanov et al. refined this approach using detailed energy-resolved mass spectrometry and systematic distance variation [6]. Their work on (V,Al)N films showed that the enhancement of room-temperature crystallinity correlates primarily with the increase in potential energy input. Notably, applying a DC bias to increase kinetic energy by approximately 30 eV did not produce the same crystallization effect, even though it increased the total ion energy. This demonstrated that potential energy plays a distinct role in promoting film crystallinity. Crucially, Kalanov et al. addressed the flux-energy coupling by varying the source-to-substrate distance from 8 to 20 cm: moving the substrate further away reduced the ion flux while maintaining similar ion charge states and energies, enabling direct comparison of potential energy effects at almost identical flux levels.

Despite these advances, key questions remain for extending this framework to other material systems. Both studies explored the effects of activated nitrogen in reactive deposition, which consists of both ionized and neutral (but excited) nitrogen species [3, 7]. While Unutulmazsoy et al. [5] focused on reactive deposition with nitrogen and Kalanov et al. [6] examined both metallic and reactive modes, a key question remains unanswered: what fraction of the activated nitrogen (nitrogen participating in the plasma process) consists of neutral species versus ionized species? This distinction is crucial for understanding the relative contributions of ions and neutrals to film growth, particularly in reactive mode where both species can participate in nitride formation.

For TiAlN specifically, which benefits from greater natural abundance and lower cost than vanadium-based nitrides, while comparative studies between cathodic arc and magnetron sputtering have shown that ion energy flux significantly affects texture

and mechanical properties [8], the flux-energy decoupling framework established for (V,Al)N has not been applied to this industrially important system.

### 1.3 Objectives

This thesis addresses above mentioned gaps in literature by systematically investigating the role of ion flux in Ti–Al–N thin film growth via pulsed filtered cathodic arc deposition. The specific objectives are:

1. Characterize the ion flux and the total flux (flux of all particles arriving at the substrate) as a functions of external magnetic field strength and distance from the macroparticle filter. Furthermore, analyse the ion energy distributions of individual ionic species.
2. Investigate the sweet spot from metallic to reactive mode by varying nitrogen pressure and quantify how this affects the ion-to-neutral ratio arriving to the substrate.
3. Establish quantitative correlations between ion flux and total flux across the experimental parameter space of magnetic field, nitrogen pressure, and distance from the macroparticle filter.
4. Characterize the crystallinity, film thickness, film composition of deposited TiAlN films at selected process parameters with film properties.

The experimental approach combines multiple *in situ* plasma diagnostics with *ex situ* film characterization to extend the framework [5, 6] to both reactive mode operation and the industrially relevant TiAlN system. This multi-diagnostic strategy, applied across a systematic parameter space, enables investigation of two key aspects: (1) explore room temperature deposition of TiAlN films, and (2) the combined measurement of ion flux versus total deposited flux to distinguish the contribution of non-ionized activated nitrogen species and forming thin film structure.

# CHAPTER 2

---

## Theoretical Background

---

### 2.1 Plasma generation and composition

#### 2.1.1 Cathode spot plasma generation

Cathodic arc plasmas form at microscopic emission centers, known as cathode spots, on an otherwise cold metal electrode under vacuum. Spot ignition occurs when the local cathode surface, through breakdown of adsorbates or field-enhanced thermionic emission, undergoes explosive release of electrons and vaporized metal. During a single spot pulse, a few nanograms of the cathode material rapidly heat up, vaporize and ionize. This produces a dense, quasineutral plasma plume composed mostly of metal ions and electrons. The peak spot current densities reach  $10^{10}$ – $10^{12} \text{ A m}^{-2}$ , far above steady-state thermionic or field emission limits. These microexplosions, termed as ectons (explosive electron emission centers), were first described by Mesyats [9] and produce localized nanosecond-scale plasma bursts. The arc plasma is sustained by repetitive ecton events occurring at or near the same location [3, Chap. 3.3–3.4].

The spot-generated plasma exhibits two defining characteristics. First, the extreme power density at the cathode spot produces a high degree of ionization, with more than 90% of the ejected metal atoms emerging as ions [3, Chap. 3.5]. Second, the high electron temperature and density in the spot plasma generate multiply charged ions, with charge state distributions extending to  $Q = 3$ – $4$  for refractory metals such as Ti and Al [3, Chap. 3.5].

Spot ignition and quenching occur on timescales of 10–100 ns, with each pulse eject-

ing a fully ionized burst of metal vapour. The sustained arc discharge thus consists of continuously overlapping microplasma pulses, producing a metal-rich, high-flux ion stream well-suited for energetic thin-film deposition.

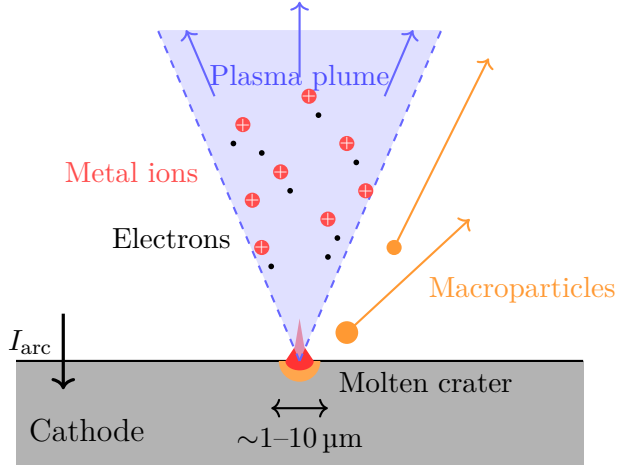


**Figure 2.1.** Schematic of cathode spot operation. The arc current  $I_{\text{arc}}$  concentrates at a microscopic spot ( $1-10 \mu\text{m}$ ), creating a molten crater from which a plasma plume of metal ions, electrons and macroparticles expand. Adapted from [10]

### 2.1.2 Pulsed versus continuous arc operation

Cathodic arcs can operate in either continuous (DC) or pulsed mode, with fundamental differences in plasma generation dynamics. In DC operation the cathode spot moves continuously across the surface, maintaining a steady-state plasma density determined by the balance between plasma generation at the spot and losses through expansion. The time-averaged plasma properties remain constant, and the ion flux to the substrate is continuous.

In pulsed operation, the arc is periodically initiated and extinguished, creating discrete plasma bursts separated by periods with no plasma generation. During the active phase of each pulse, the instantaneous plasma density can be significantly higher than in DC arcs operating at the same average power, because the energy is concentrated in short time intervals. The peak plasma density scales with the instantaneous arc current. Between pulses the plasma expands and dissipates, allowing the cathode surface to cool. This temporal modulation affects both the spot dynamics and the resulting plasma composition.

The ion charge state distributions in pulsed arcs are typically similar to or slightly enhanced compared to DC arcs, as the higher instantaneous power density can promote additional ionization events in the cathode spot region [3, Chap. 10].

### 2.1.3 Plasma expansion and macroparticle filtering

Following their generation at the cathode spots, the plasma bursts expand into the vacuum chamber. This expansion is supersonic, with ions carrying directed kinetic energy away from the cathode. In many industrial and research systems, the expanding plasma is guided through a magnetic filter that removes macroparticles while allowing plasma to pass along curved magnetic field lines.

In the region near the cathode (within a few centimetres of the spot), plasma densities are on the order of  $10^{18} \text{ cm}^{-3}$  and electron temperatures  $T_e \approx 5\text{--}10 \text{ eV}$  (expressed in energy units). As the plume propagates, its density decreases according to

$$n(r) = \frac{C I_{\text{arc}}}{r^2} \quad (2.1)$$

where  $I_{\text{arc}}$  is the arc current,  $r$  the distance, and  $C$  a constant related to the ion erosion rate of the cathode material. This  $1/r^2$  scaling assumes free expansion, but deviations can occur due to magnetic fields or reactive gases, which may alter the plasma trajectory or cause recombination [3, Chap. 4.3, Eq. 4.3, p. 178].

In cathodic arc discharges from titanium cathodes, whether pure Ti or Ti-Al compounds, ions generally carry an average charge state  $\langle Q \rangle \approx 2$  at the source [3, Chap. 4.1, App. B.8]. This high degree of ionization reflects the extreme power density of the spot and follows the cohesive energy rule, which links  $\langle Q \rangle$  to the cohesive energy of the cathode material [3, App. B.8].

In the present work, a  $90^\circ$  curved magnetic filter guides the expanding plasma toward the substrate region while removing macroparticles. After passing through the filter, the plasma has evolved from its initial state at the cathode spot, having undergone expansion, potential collisions with background gas and interaction with guiding magnetic fields. The properties of this filtered plasma in the substrate region determine the energy and flux delivered to the growing film, are the focus of the following sections.

## 2.2 Ion energies and flux in the substrate region

This section focuses on the properties of ions in the plasma after expansion and filtering, in the region where they reach the substrate and form the growing film.

### 2.2.1 Ion energies: origins and implications

Ions in cathodic arc plasmas carry both kinetic and potential energy. The kinetic energy  $E_{\text{kin}}$  arises from the supersonic expansion of plasma from the cathode spot, while the potential energy  $E_{\text{pot}}$  is released upon neutralization at the substrate surface and is determined by the ionization states of the incoming ion to the substrate surface.

The total energy delivered by an ion to the growing film is

$$E_{\text{tot}} = E_{\text{kin}} + E_{\text{pot}}. \quad (2.2)$$

For cathodic arc plasmas, the kinetic energy is closely linked to the arc burning voltage, which remains nearly constant at 30–35 V [3, Chap. 4.2]. This voltage accelerates ions away from the cathode region, giving them characteristic drift velocities. As ions traverse the expanding plasma, they may undergo collisions that modify their energy distribution.

Table 2.1 summarizes characteristic ion properties for Ti and Al cathodic arc plasmas in vacuum, measured near the cathode from literature [3, App. B, Table B.8].

**Table 2.1.** Characteristic ion properties for Ti and Al cathodic arc plasmas in vacuum, near the cathode spot.

| Species          | $\langle Q \rangle$ | $E_{\text{kin}}$ (eV) | $E_{\text{pot}}$ (eV) | $E_{\text{tot}}$ (eV) |
|------------------|---------------------|-----------------------|-----------------------|-----------------------|
| Ti <sup>2+</sup> | 2.1                 | 59                    | 21                    | 80                    |
| Al <sup>2+</sup> | 1.7                 | 28                    | 24                    | 52                    |

These values, measured near the cathode spot, serve as reference for understanding the energy range of ions. In this work, the plasma is characterized after expansion and filtering, where ion energies may differ from these initial values. Nonetheless for the materials used in this work, the total ion energies are expected to exceed the approximately 30 eV threshold for subplantation, enabling densification and obtaining crystalline Ti–Al–N films without requiring external substrate heating [11].

## 2.2.2 Effect of distance on ion properties

As ions travel from the cathode through the filter and toward the substrate, their properties evolve due to geometric expansion and collisions. The ion flux decreases with the square of the distance due to the expanding plasma front as seen in Eq. 2.1.

In vacuum (metallic mode), the ion energy distributions remain relatively narrow and well-defined. At increased distances, the plasma density decreases but the relative composition and charge states are largely preserved, therefore the ion flux at the substrate position becomes an important parameter, as it determines the rate and amount at which energy is delivered to the growing film. Understanding how distance affects the ion flux provides insight into the spatial uniformity of the deposition process and allows optimization of substrate positioning.

## 2.2.3 Effect of external magnetic fields

Applying an external axial magnetic field at the arc source modifies the plasma properties in several ways. The magnetic field confines electrons near the cathode spot through their gyration around field lines, while the heavier ions are less affected and can still reach the anode. This "magnetic insulation" effect reduces electron current to the anode, requiring a higher voltage to maintain the arc current. The higher voltage accelerates ions more strongly and increases the plasma temperature in the cathode spot region, prolonging the interaction time between electrons and ions [4]. These changes lead to:

- Increased average ion charge state  $\langle Q \rangle$ , which increases the ion potential energy,
- Simultaneously increased ion kinetic energy,
- Enhanced ion flux, which can increase by up to an order of magnitude [4].

This coupling presents a challenge for isolating the individual contributions of ion energy and ion flux to film growth. Decoupling these parameters requires additional experimental approaches, such as varying the source-to-substrate distance to modulate flux while maintaining similar ion energies, or applying bias voltages to shift ion kinetic energies independently [5, 6].

## 2.2.4 Ion flux

The ion flux  $\Gamma$  represents *the number of ions arriving per unit area per unit time*, expressed in  $\text{ions cm}^{-2} \text{s}^{-1}$ . In a cathodic arc plasma, the total ion current density  $J_i$

(A cm<sup>-2</sup>) relates to  $\Gamma$  via

$$\Gamma = \frac{J_i}{e \langle Q \rangle}, \quad (2.3)$$

where  $e$  is the elementary charge and  $\langle Q \rangle$  the average ion charge state.

In vacuum cathodic arcs, the burning voltage remains nearly constant at 30–35 V for arc currents, so the plasma generation rate and thus  $\Gamma$  increases approximately linearly with the arc current  $I_{\text{arc}}$  [3, Chap. 6.5]. The absolute ion flux at the substrate depends not only on the arc current but also on the distance from the source and the presence of magnetic fields or reactive gases. These factors determine the fraction of plasma reaching to the substrate and its composition which may be different than generated plasma at the source. The transition from metallic to reactive process introduces additional complexity, as discussed in the following section.

## 2.3 Reactive process and nitrogen activation

### 2.3.1 Transition from metallic to reactive mode

Cathodic arc deposition operates in two distinct regimes. In metallic mode, the cathode surface remains metallic and the plasma consists exclusively of metal ions, characterized by high ionization degrees. In reactive mode, a background gas such as N<sub>2</sub> adsorbs onto the cathode surface, forming a compound layer that poisons the cathode and alters both spot behaviour and plasma composition [3, Chap. 9.2].

When N<sub>2</sub> is introduced, a dynamic equilibrium develops between compound formation (through adsorption and reaction at the cathode surface) and compound removal (via explosive ejection events that eject both metal and nitrogen containing particles) [3, Chap. 9.3]. The equilibrium position depends on gas pressure, arc current, and cathode composition. At low N<sub>2</sub> pressures or high power densities, type-2 (metal-rich) spots prevail maintaining predominantly metal ion flux. At higher pressures, type-1 (poisoned) spots dominate producing a mixed plasma of metal and nitrogen ions [3, Chap. 9.4]. This transition affects not only the chemical composition of the deposited film but also the energy distribution and charge state distribution of the plasma, as compound formation at the cathode alters the electron emission and plasma generation mechanisms.

### 2.3.2 Activated nitrogen species

In reactive mode, the plasma contains not only metal ions but also activated nitrogen species. These include:

- Ionized nitrogen:  $\text{N}^+$  and  $\text{N}_2^+$  ions formed by electron-impact ionization,
- Neutral but excited nitrogen: metastable  $\text{N}_2$  and atomic N species that carry internal energy but no net charge.

The term “activated nitrogen” encompasses both ionic and neutral excited species that participate in film growth. While ionized species can be detected directly by mass spectrometry, the contribution of neutral activated species is more difficult to quantify. This distinction is important because the total deposited flux includes both ionic and neutral components, whereas ion current measurements detect only the charged fraction.

Charge exchange with  $\text{N}_2$  reduces the average charge state of metal ions and introduces gas-ion species, altering the potential energy delivered to the film [3, Chap. 9.4]. Collisions during plasma expansion also reduce ion drift velocities, lowering kinetic energy before it hits the substrate. These events collectively modify the available energy for film growth in reactive mode compared to metallic mode. The interplay between metal ion flux, activated nitrogen flux, and their respective energies determines the resulting film composition, structural properties, as discussed in the following section.

## 2.4 Plasma–surface interactions and film growth

### 2.4.1 Energetic condensation and subplantation

When metal ions with sufficient energy strike the growing film, they penetrate below the surface and deposit energy through a shallow collision cascade. This subplantation process produces two key effects:

- **Localized densification:** Ions with energies above approximately 30 eV implant beneath the surface, occupying interstitial sites and displacing near-surface atoms through knock-on collisions. This reduces porosity and increases film density, which is important for transition-metal nitride coatings such as Ti–Al–N [11].
- **Atomic-scale heating:** The deposition of kinetic energy and release of potential energy (neutralization) generate localized, nanosecond-scale temperature spikes. These enhance adatom mobility and promote crystallite coalescence without requiring global substrate heating [3, Chap. 8.2].

As the energetic input from ions increases, films transition from porous, amorphous structures to dense, crystalline coatings. This densification introduces compressive

stresses of several GPa through atomic peening [3, Chap. 8.1–8.4]. For example, TiN films grown with total ion energies of approximately 60 eV develop a preferred cubic (111) texture and hardness exceeding 30 GPa [2].

The relationship between ion flux and film growth rate is dependent on

$$R = \frac{m_{\text{ion}} \Gamma S}{\rho_{\text{film}}}, \quad (2.4)$$

where  $m_{\text{ion}}$  is the average ion mass,  $\Gamma$  the ion flux,  $S$  the sticking coefficient, and  $\rho_{\text{film}}$  the film density. The sticking coefficient  $S$  represents the probability that an arriving ion incorporates into the growing film rather than being reflected or resputtered. For metal ions at moderate energies  $S \approx 1$  (below the resputter threshold of approximately 100–200 eV) [3, Chap. 8.3]. In contrast the film density  $\rho_{\text{film}}$  itself depends on the ion energy and flux, as higher energies promote densification through subplantation. This interdependence between flux, energy, and resulting film structure motivates the systematic study of these parameters, which is the focus of this work.

## 2.4.2 Structure-zone models

The microstructure of thin films deposited by physical vapour deposition depends strongly on the energy and flux of incident species. Thornton’s structure-zone model was originally developed for magnetron sputtering and relates film morphology to the homologous temperature  $T/T_m$  (substrate temperature normalized to the melting point) and working gas pressure [12]. At low  $T/T_m$  and high pressures, films exhibit porous, columnar structures (Zone 1) due to limited adatom mobility. As  $T/T_m$  increases denser columnar (Zone T) and eventually equiaxed crystalline structures (Zone 2 and Zone 3) develop.

Anders extended this framework to account for the energetic ion bombardment characteristic of cathodic arc deposition [13]. In the revised model, ion energy  $E^*$  (normalized to a displacement energy) replaces gas pressure as the second axis, reflecting the dominant role of ion bombardment in densification of thin films. High-energy ions can induce subplantation and atomic peening even at low substrate temperatures, enabling dense and crystalline films without external heating, which is a key advantage of energetic deposition methods, particularly cathodic arc processes. However, excessive ion energy leads to lattice damage, defect accumulation and eventually amorphization or resputtering, defining an optimal energy window for film growth [3, Chap. 8.3].

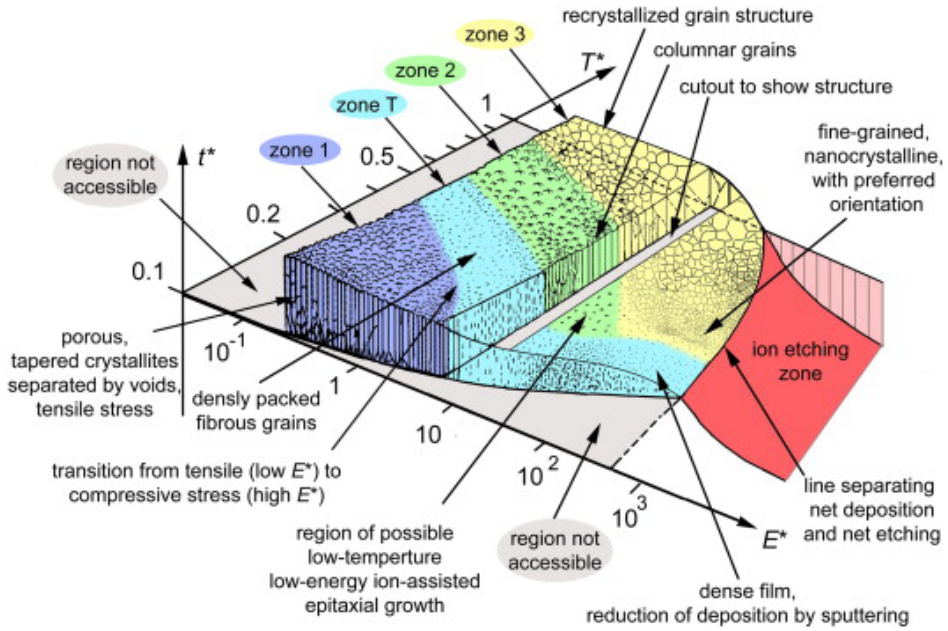


**Figure 2.2.** Structure-zone diagram for plasma based thin film deposition, showing film microstructure as a function of generalized temperature  $T^*$  and normalized ion energy  $E^*$ . Image taken from Anders' work [13].

### 2.4.3 TiAlN crystal structures

Titanium aluminium nitride ( $\text{Ti}_{1-x}\text{Al}_x\text{N}$ ) coatings are widely used for wear protection and cutting tools. The crystal structure depends primarily on the aluminium content  $x$ :

- For  $x \lesssim 0.6\text{--}0.7$ ,  $\text{Ti}_x\text{Al}_{1-x}\text{N}$  crystallizes in the metastable cubic B1 structure, where Al atoms substitute for Ti on the metal sublattice. This cubic phase exhibits hardness values of 25–35 GPa and is the preferred structure for most industrial applications [1].
- For  $x \gtrsim 0.7$ , the stable wurtzite (B4) structure becomes dominant. The wurtzite phase has lower hardness (typically 15–20 GPa) and is generally undesirable for hard coating applications [2].
- At intermediate compositions, mixed cubic-wurtzite structures or nanocomposite arrangements may form depending on deposition conditions.

The metastable cubic phase cannot be synthesized by all deposition methods. Conventional sputtering typically requires elevated substrate temperatures to achieve cubic-phase growth at high Al contents. In contrast, energetic deposition techniques such as cathodic arc evaporation or hybrid high-power impulse magnetron sputtering combined with DC magnetron sputtering enable room-temperature synthesis of the cubic phase by providing sufficient kinetic and potential energy for atomic rearrangement without relying on thermal diffusion [14]. This energetic bombardment extends the solubility

limit of Al in the cubic phase beyond the thermodynamic equilibrium value.

The cathode composition used in this work (75 wt.% Ti – 25 wt.% Al) is expected to produce cubic-phase  $\text{Ti}_{1-x}\text{Al}_x\text{N}$  films under typical cathodic arc conditions.

# CHAPTER 3

---

## Experimental Methodology

---

This chapter describes the experimental apparatus, diagnostic techniques, and data processing methods used to investigate the correlation between ion flux and mass deposition rate in pulsed filtered cathodic arc deposition of Ti–Al–N thin films. The approach combines three complementary in-situ diagnostics: a Langmuir probe for ion current measurements, a quartz crystal microbalance (QCM) for real-time mass deposition monitoring, and an energy-resolving mass spectrometer (ERMS) for charge-state-resolved ion energy distributions.

Plasma was generated using a water-cooled cylindrical anode and a rod cathode with composition 75 wt.% Ti; 25 wt.% Al (corresponding to 62.8 at.% Ti; 37.2 at.% Al). The cathode had a diameter of 6.35 mm and length of 38.1 mm. The expanding plasma was guided through a 90° curved magnetic macroparticle filter connected in series with the arc source.

### 3.1 Experimental setup

#### 3.1.1 Vacuum & gas control

The vacuum chamber was evacuated using a two-stage pumping system consisting of a dry rotor vacuum pump (Leybold ECODRY+) for roughing and a cryogenic pump (Leybold COOLVAC) for the main pumping line, achieving a base pressure on the order of  $1 \times 10^{-5}$  Pa with the cryopump fully open. To control the working pressure during reactive deposition, the cryopump gate valve was partially closed to position 345 (approximately 34.5% open), which reduced the effective pumping speed and increased

the base pressure to approximately  $1 \times 10^{-4}$  Pa.

Nitrogen gas ( $\text{N}_2$ , 99.999% purity) was introduced via a mass flow controller (MKS IO Type B), with chamber pressures monitored using a Pfeiffer PKR 361. The nitrogen flow rate of 1 to 12.8 sccm (standard cubic centimeters per minute) leads to nitrogen partial pressures between 0.025 and 0.3 Pa.

### 3.1.2 Power circuits and arc operation

The arc power supply (Melec SPIK3000A) operated in pulsed DC mode, delivering arc currents up to 450 A at pulse frequencies ranging from 0.2 to 5 Hz, with a typical pulse width of 1 ms. The arc current was monitored using a Chauvin Arnoux MA200 connected to a Tektronix MSO64 oscilloscope. The cathode voltage relative to ground and anode voltage were measured on additional channels to determine the burning voltage during the pulse.

A coil wound around the cylindrical anode (EM-coil) was used to minimize the losses of the ion charge states leaving the source through magnetic confinement (see Section 2.2.3). This coil was connected to a separate pulsing unit (Melec SPIK3000A) capable of delivering currents up to 850 A. The EM-coil was triggered 200  $\mu\text{s}$  before arc ignition to ensure the magnetic field reached stable conditions before plasma generation. The coil current was monitored using another Chauvin Arnoux MA200, with a typical pulse width of 1.5 ms.

The magnetic field strength within the EM-coil solenoid was estimated using:

$$B = \frac{\mu_0 N I}{L} \quad (3.1)$$

where  $L = 0.02$  m is the solenoid length,  $N = 5$  is the number of turns,  $\mu_0 = 1.256 \times 10^{-6} \frac{\text{T}\cdot\text{m}}{\text{A}}$  is the vacuum permeability, and  $I$  is the peak coil current. The peak current was determined from oscilloscope measurements at the beginning of the pulse, as this represents the maximum field strength before resistive losses cause the current to decay. The current waveform drops within a pulse due to the design of the pulsing unit in the power supplies. Figure 3.1 shows exemplary current waveforms for both the arc and EM-coil for a 250 V input to the coil power supply. An additional example for 100 V input is provided in Appendix B.1.

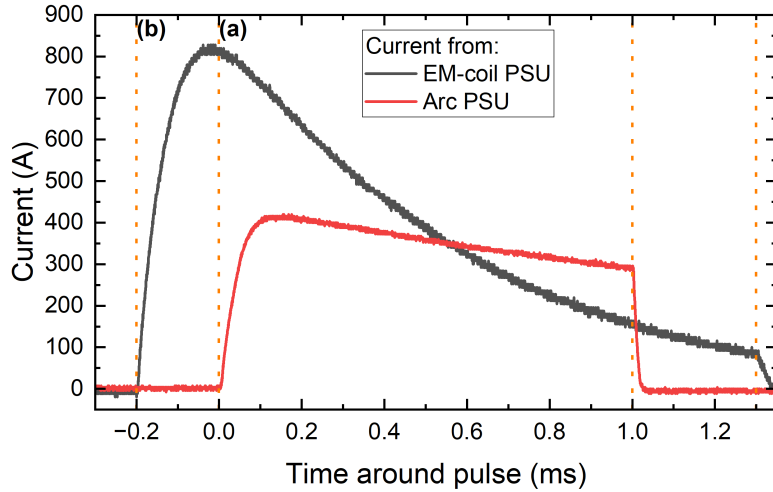


**Figure 3.1.** Example pulse waveforms showing the arc current (red) and EM-coil current (black) as a function of time. The orange dashed lines indicate the trigger timing: (a) EM-coil trigger at  $t = -0.2$  ms, (b) arc trigger at  $t = 0$  ms. The waveforms shown here are pulses at 250 V EM-coil input voltage. Distance: 10 cm, pressure: 0 Pa of N<sub>2</sub>, magnetic field: 0.25 T.

### 3.1.3 Diagnostic positioning and synchronization

A delay generator (Stanford Research Systems DG645) served as the master clock for the experimental system, providing precisely timed trigger signals to:

- the arc power supply (channel **a**),
- the EM-coil power supply (channel **b**),
- the energy-resolving mass spectrometer (channel **c**).

The oscilloscope was triggered on the rising edge of the cathode voltage (channel 1), which marks the onset of the arc pulse. Channels 1 and 2 of the oscilloscope measured the cathode-to-ground voltage and anode-to-ground voltage, respectively. Channels 3 and 4 recorded the arc current and EM-coil current via current probes. The ion current was recorded separately, more on that in Section 3.2.1.

The vacuum chamber setup for cathodic arc plasma diagnostics and thin film deposition is shown in Figure 3.2. The green arrow illustrates the trajectory of the plasma plume as it expands from the cathode, passes through the 90° macroparticle filter, and reaches the target. This experimental configuration enabled systematic investigation of plasma properties and film growth as functions of distance, magnetic field strength, and nitrogen pressure, as detailed in the following sections.

The ion current probe and quartz crystal microbalance (QCM) were not triggered by the delay generator. The ion probe signal was recorded directly by the oscilloscope

(triggered on the cathode voltage), automatically synchronizing ion current measurements with the arc pulses. The QCM operated continuously, with frequency measurements recorded before and after each sputtering run to determine the accumulated mass change over a fixed number of pulses. The BNC cable connector was detached during sputtering, this was done to protect the sensitive components in the oscillator from the highly energetic plasma.

For in situ plasma diagnostics, the Langmuir probe and QCM were mounted on a custom movable assembly positioned at distances ranging from 10 to 20 cm from the macroparticle filter exit. The energy-resolving mass spectrometer (ERMS) was mounted on a separate linear feedthrough allowing independent adjustment of its position (distance from the filter exit) for spatial characterization of the plasma. Film depositions were performed using silicon substrates mounted on a third movable holder, also positioned at controlled distances from the filter exit.

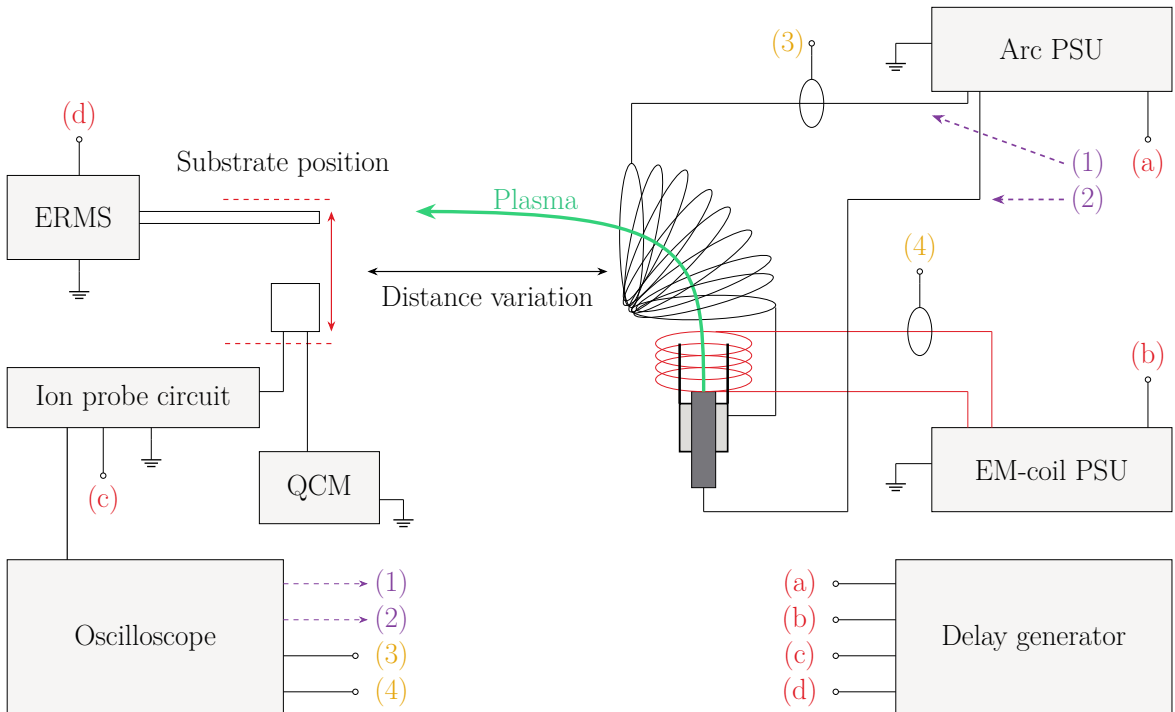


**Figure 3.2.** Schematic of the vacuum chamber setup for cathodic arc plasma diagnostics and thin film deposition with the plasma originating from the cathode (dark grey) and a trajectory through the EM-coil and the macroparticle filter shown in green. At the substrate position the ERMS could be pulled back, allowing either the substrate holder or a custom holder assembly integrating the ion current probe and QCM (Fig. A.1) to be placed into the plasma trajectory (red double sided arrow). The delay generator synchronizes both PSUs, the ERMS (when used) and the biasing for the ion current probe, and the oscilloscope records all the data as described in Sec.3.1.3.

## 3.2 Plasma diagnostics

### 3.2.1 Ion current probe

An in-house-built ion collector probe was designed to measure the ion current density in ion saturation mode. The probe was a 5 mm diameter copper rod machined into a nail-head shape. This design prevented short circuits between the probe and the grounded mount due to metallic deposition. The probe body was wrapped in Kapton tape for electrical insulation from the aluminum mounting assembly (Figure A.1).



**Figure 3.3.** In-house built ion collector probe wrapped in Kapton tape for electrical insulation from the aluminum assembly holder. The probe includes an attachment point for a screw terminal connector, enabling connection to the ion probe circuit.

To ensure full ion collection and suppress electron current, the probe was negatively biased at  $V_b = -80$  V to operate in the ion saturation regime [15], as determined through bias voltage characterization measurements (Appendix A.5).

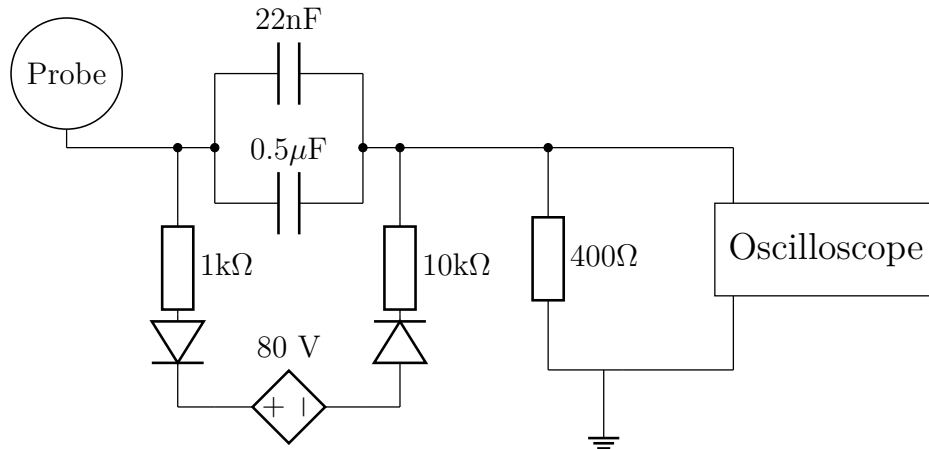


**Figure 3.4.** Schematic of the ion-flux probe circuit. The  $400\Omega$  resistor converts ion current to voltage, while the  $0.5\mu\text{F}$  capacitor and  $400\Omega$  resistor form a high-pass filter with a 795 Hz cutoff.

The probe circuit (Figure 3.4) converts the collected ion current to a voltage signal. The ion current passes through a  $0.5\mu\text{F}$  coupling capacitor and develops a voltage across the  $400\Omega$  measurement resistor. This RC configuration forms a high-pass filter with cutoff frequency:

$$f_c = \frac{1}{2\pi RC} = \frac{1}{2\pi \cdot 400 \Omega \cdot 0.5 \times 10^{-6} F} \approx 795 \text{ Hz} \quad (3.2)$$

The high-pass filter blocks DC offsets while passing the pulsed ion current signal. The RC time constant  $\tau = 200 \mu\text{s}$  is much shorter than the 2 s interval between pulses, ensuring complete capacitor discharge between measurements. The bias supply line incorporates a 22 nF capacitor and 1 k $\Omega$  resistor as a low-pass filter to smooth the -80 V bias voltage.

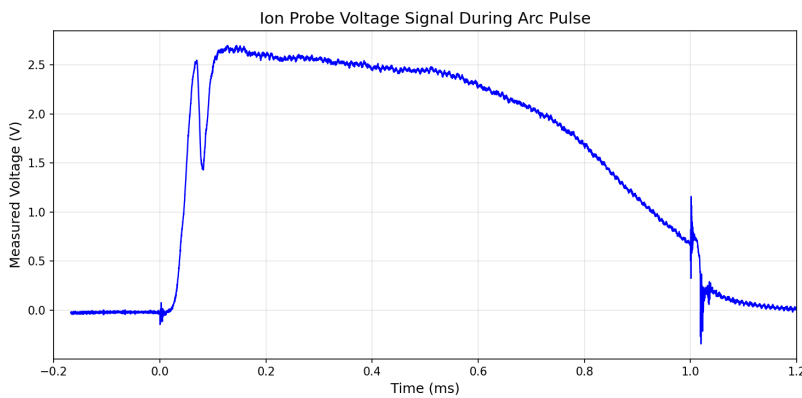


**Figure 3.5.** Example voltage waveform measured across the 400  $\Omega$  resistor during a single arc pulse. The signal shows transients at pulse ignition (0 ms) and termination (1 ms), with gradual decay during the pulse due to the high-pass filter characteristics.

The ion current is calculated from the measured voltage as:

$$I_{\text{ion}} = \frac{V_{\text{measured}}}{R} \quad (3.3)$$

The voltage signal was recorded using a Tektronix MSO64 oscilloscope. Figure 3.5 shows an example waveform of 64 pulses averaged. The ion current density  $J_i$  is calculated as:

$$J_i = \frac{V_{\text{measured}}}{A \cdot R} \quad (3.4)$$

where  $A = 0.196 \text{ cm}^2$  is the probe collection area and  $R = 400 \Omega$ .

### 3.2.2 Quartz crystal microbalance

A quartz crystal microbalance (QCM) was used to measure the deposited mass during pulsed cathodic arc operation. The system consisted of an INFICON Cool Drawer<sup>TM</sup> with a single sensor in standard orientation and water cooled to ensure thermal stability. A 14 mm diameter, 6 MHz AT-cut quartz crystal was operated with an SQM-160

controller for electronic readout.

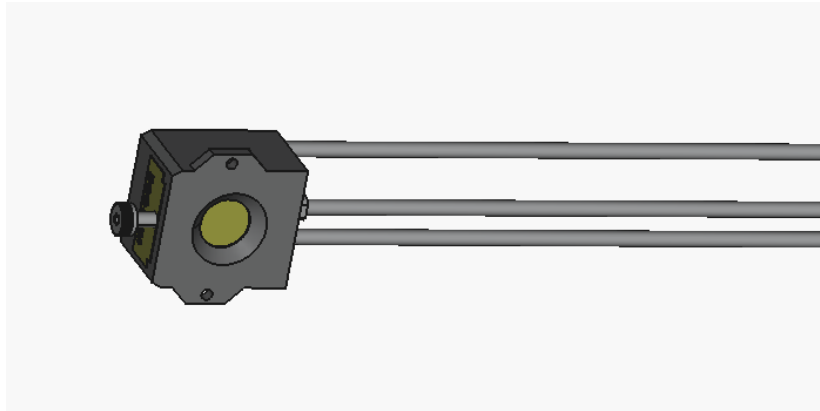


**Figure 3.6.** Sensor head of the INFICON Cool Drawer™ Quartz Crystal Microbalance (QCM) used for in-situ mass operation monitoring during cathodic arc sputtering. The assembly includes a water-cooled housing, a 14 mm diameter AT-cut quartz crystal (6 MHz), and electrode leads for connection to the SQM-160 controller. (Schematic is adapted from INFICON STP file, available at <https://www.inficon.com/en/products/thin-film-technology/cool-drawer-single-sensor>).

The measurement principle follows the Sauerbrey equation [16], which relates the change in resonance frequency of the quartz crystal to the deposited mass:

$$\Delta m = \frac{N_{\text{AT}} \rho_q \pi r^2}{F_q^2} \Delta F = 18.8146023 \times 10^{-9} \frac{\text{g}}{\text{Hz}} \cdot \Delta F \quad (3.5)$$

Here  $\rho_q = 2.649 \text{ g cm}^{-3}$  is the quartz density,  $r = 0.7 \text{ cm}$  is the radius of the crystal area,  $N_{\text{AT}} = 166 \text{ 100 Hz cm}$  is the frequency constant of the AT-cut quartz,  $F_q = 6 \text{ MHz}$  is the uncoated resonance frequency, and  $\Delta F$  is the measured frequency shift.

The Sauerbrey relation is accurate as long as  $\Delta F \lesssim 0.05 F_q$  (approximately 0.3 MHz for a 6 MHz crystal), details on the correction above this limit is given in Appendix A.1. In the present experiments, the observed frequency shifts ranged from approximately 1 Hz to 50 Hz over 64 pulses. These shifts are well above the SQM-160 resolution of approximately 0.03 Hz at 6 MHz, yet orders of magnitude below the Sauerbrey breakdown limit. The Sauerbrey approximation was therefore fully sufficient for all measurements in this work.

### 3.2.3 Simultaneous ion probe and QCM measurements

To enable direct comparison between ion current and deposited mass, the Langmuir probe and QCM were mounted on the same movable aluminum assembly. The probe

was positioned through a precision-milled pass-through hole, while the QCM was secured in a dedicated cutout and fixed via screws (see Appendix A.2 for assembly details). This configuration ensured rigid mechanical alignment between the two diagnostics throughout all measurements.

The probe collection area ( $A_{\text{probe}} = 0.196 \text{ cm}^2$ , diameter 5 mm) was smaller than but contained within the QCM crystal area ( $A_{\text{QCM}} = 1.54 \text{ cm}^2$ , diameter 14 mm). Both diagnostics were positioned as close as possible to each other to minimize spatial gradients between measurement locations. This design is meant to mitigate radial plasma density gradients inherent to expanding cathodic arc plasmas [3, Chap. 6.2], though even with close proximity, gradients cannot be completely eliminated and remained evident in the experimental results.

### 3.2.4 Energy-resolving mass spectrometer (ERMS)

An energy-resolving mass spectrometer (ERMS, Hiden EQP 1000) was used to measure ion energy distribution functions (IEDFs) and charge-state-resolved fluxes of plasma species. The system combines an electrostatic energy analyzer with a quadrupole mass filter to measure distributions of energy-to-charge ratios (E/Q) at fixed mass-to-charge ratios (M/Q), and vice versa.

Ions enter the ERMS through a  $50 \mu\text{m}$  sampling orifice and are transported to the energy analyzer, where their kinetic energy  $E_i$  is selected according to:

$$E_i = \left( V_{\text{ENERGY}} + \frac{R}{d} V_{\text{PLATES}} - V_{\text{AXIS}} \right) Q \cdot e \quad (3.6)$$

Here,  $V_{\text{ENERGY}}$  and  $V_{\text{AXIS}}$  are opposing potentials applied to the analyzer,  $R$  is the mean radius of the cylindrical sector,  $d$  is the plate separation,  $V_{\text{PLATES}}$  is the potential difference across the sector plates,  $Q$  is the ion charge state, and  $e$  is the elementary charge [17].

The energy-selected ions are then injected into the quadrupole mass filter, where a combination of AC and DC electric fields creates a stability region dependent on  $M/Q$ , described by the Mathieu equations [18]. The potential in the quadrupole is:

$$V(x, y, t) = \frac{U_0 \cos(\omega t)}{r_0^2} (x^2 - y^2) \quad (3.7)$$

where  $U_0$  is the amplitude of the AC voltage,  $\omega$  is the angular frequency, and  $r_0$  is the field radius. The stability of ion motion is determined by the dimensionless

parameters:

$$a = \frac{8eU_{DC}}{Mr_0^2\omega^2}, \quad q = \frac{4eU_0}{Mr_0^2\omega^2} \quad (3.8)$$

with  $U_{DC}$  as the superimposed DC voltage and  $M$  the ion mass. For a given  $M/Q$ , stable transmission occurs only within specific  $(a, q)$  regions, enabling mass separation [18, 19]. Only ions with trajectories stable in both radial and axial directions reach the detector.

To reduce interference from the arc's magnetic field, the ERMS was equipped with a grounded mu-metal shield [4].

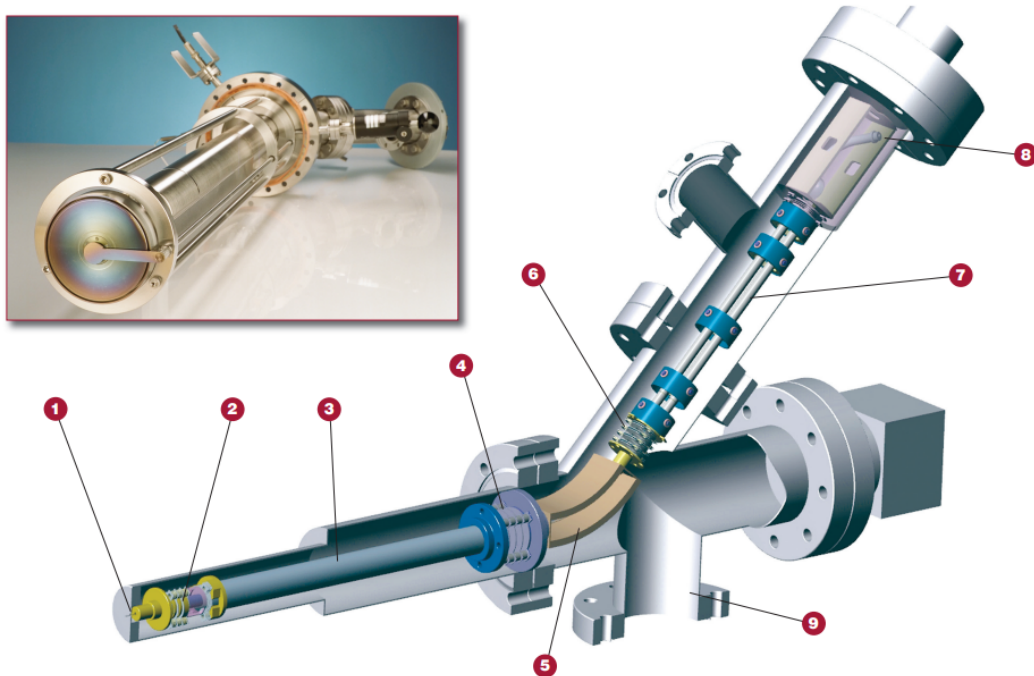


**Figure 3.7.** ERMS, Hiden EQP HE 1000: (1) Sampling Orifice, (2) Electron Impact Ion Source, (3) Transfer Ion Optics, (4) Quadrupole Lens, (5) Energy Filter, (6) Decelerating Lens, (7) Quadrupole Mass Filter, (8) Detector, (9) Differential Pump Port [20]

IEDFs were measured using a double-trigger acquisition scheme synchronized with the arc pulses (1 ms duration, 5 Hz repetition rate). For each  $M/Q$  value, two 20 ms acquisition windows were recorded, initiated 10 ms before the onset of the pulse. The combined 40 ms of data for each point were averaged to obtain the final IEDF. Measurements were performed for charge states  $1^+$ ,  $2^+$ , and  $3^+$  of aluminum ions, and for charge states  $1^+$ ,  $2^+$ ,  $3^+$ , and  $4^+$  of titanium ions. For nitrogen ion species ( $N$  and  $N_2$ ), only the  $1^+$  ionization level was measured. This was achieved by scanning  $V_{ENERGY}$  while fixing the quadrupole mass filter to the corresponding  $M/Q$  values (Table 3.1).

**Table 3.1.** Mass-to-charge ratios measured for each ion species and charge state.

| Charge state | Al         | Ti     | N  | N <sub>2</sub> |
|--------------|------------|--------|----|----------------|
|              | (M/Q, amu) |        |    |                |
| 1+           | 27         | 47.867 | 14 | 28             |
| 2+           | 13.5       | 23.933 | –  | –              |
| 3+           | 9          | 15.955 | –  | –              |
| 4+           | –          | 11.966 | –  | –              |

### Energy Conversion and Mass Transmission Correction

The ERMS system measures energy-per-charge ( $E/Q$ ) distributions for each mass-to-charge ratio ( $M/Q$ ). To derive ion energy distributions for different charge states, the measured  $E/Q$  distributions are converted to actual ion energies by multiplication with the corresponding charge state number  $Q$ :

$$E = Q \cdot (E/Q) \quad (3.9)$$

This conversion accounts for the charge-dependent scaling of ion energies and is necessary because the electrostatic energy analyzer resolves ion energy per unit charge, not total ion energy [17, 18].

A critical aspect of quantitative mass spectrometry is accounting for the mass-dependent transmission efficiency of the quadrupole mass filter and detector assembly. The transmission function  $T(M/Q)$  varies with mass-to-charge ratio due to the quadrupole's RF/DC field configuration and detector efficiency [7, 19]. Correction factors were determined through calibration measurements and applied to the raw ion signal intensities  $I_{\text{raw}}$  to obtain corrected intensities:

$$I_{\text{corrected}}(M/Q) = \frac{I_{\text{raw}}(M/Q)}{T(M/Q)} \quad (3.10)$$

Without this correction, lighter ions would be systematically underestimated relative to heavier ions, leading to errors in charge state distributions and composition analysis. From the corrected ion signals, statistical parameters are extracted for each charge state and species: mean ion energy  $\langle E \rangle$ , standard deviation  $\sigma_E$  characterizing the energy spread, and peak energy  $E_{\text{peak}}$  [3].

### Mean Charge State and Energy Calculations

The measured ion energies represent the kinetic energy of the ions. For each element, three key quantities are calculated from the charge-state-resolved measurements: mean charge state, mean kinetic energy, and mean potential energy.

**Mean charge state:** The mean charge state is calculated as a weighted average over all detected charge states:

$$\langle Q \rangle = \frac{\sum_Q Q \cdot I_Q}{\sum_Q I_Q} \quad (3.11)$$

where  $Q$  ranges over the detected charge states (1, 2, 3 for Al; 1, 2, 3, 4 for Ti) and  $I_Q$  is the integrated ion current for charge state  $Q$  after mass transmission correction. This is implemented by summing the IEDF over energy for each charge state to obtain:

$$I_Q = \int \text{IEDF}(E, Q) dE \quad (3.12)$$

then calculating the weighted average using the normalized weights  $w_Q = I_Q / \sum I_Q$ .

**Mean kinetic energy:** For each element, the mean kinetic energy is calculated as a weighted average over all charge states:

$$\langle E_{\text{kin}} \rangle = \frac{\sum_Q I_Q \cdot \langle E \rangle_Q}{\sum_Q I_Q} \quad (3.13)$$

where  $\langle E \rangle_Q$  is the mean energy measured for charge state  $Q$ , calculated as:

$$\langle E \rangle_Q = \frac{\int E \cdot \text{IEDF}(E, Q) dE}{\int \text{IEDF}(E, Q) dE} \quad (3.14)$$

This double-weighted approach first averages over the energy distribution within each charge state, then averages across charge states weighted by their relative abundances.

**Mean potential energy:** The potential energy associated with each charge state is calculated from the cohesive energy and ionization potentials of the cathode material, following the methodology of Kalanov et al. [6]:

$$E_{\text{pot},Q} = E_{\text{coh}} + C \sum_{i=1}^Q E_{\text{ion},i} \quad (3.15)$$

where  $E_{\text{coh}}$  is the cohesive energy (4.85 eV for Ti, 3.39 eV for Al),  $E_{\text{ion},i}$  are the successive ionization energies, and  $C$  is a factor that accounts for the fraction of ionization energy deposited in the solid, with the remainder lost through radiation and Auger electron emission. Following Kalanov et al.,  $C = 0.8$  is used, representing the energy fraction contributing to atomic-scale heating during film growth. The mean potential energy for each element is then calculated as a weighted average over charge states:

$$\langle E_{\text{pot}} \rangle = \frac{\sum_Q I_Q \cdot E_{\text{pot},Q}}{\sum_Q I_Q} \quad (3.16)$$

using the same weights  $w_Q = I_Q / \sum I_Q$  as for the charge state and kinetic energy calculations.

These three quantities are interdependent through the charge state distribution: changes in  $\langle Q \rangle$  directly affect  $\langle E_{\text{pot}} \rangle$  while  $\langle E_{\text{kin}} \rangle$  depends on the energy distribution of each charge state present. The total ion energy  $E_{\text{tot}} = E_{\text{kin}} + E_{\text{pot}}$  is used in the analysis of film growth mechanisms (Chapter 5). Implementation details of the data processing workflow are provided in Appendix A.3.

### 3.3 Thin film deposition and characterization

Thin films were deposited on Si (100) substrates mounted on a movable substrate holder positioned at controlled distances from the macroparticle filter exit. Prior to deposition, the 2x2 cm substrates were cut into four pieces and cleaned with compressed nitrogen gas. For thickness measurements, a masking technique was employed: a marker line was drawn near the edge of each substrate before deposition, creating a well-defined step edge. After deposition, this marker was removed by ultrasonic cleaning in isopropanol, leaving a sharp boundary between the coated and uncoated regions for profilometry.

The deposition parameters (distance, magnetic field strength, nitrogen pressure) were selected to match a subset of the plasma diagnostic measurements, enabling direct correlation between plasma properties and film characteristics. All depositions were performed with 6000–8000 pulses at 5 Hz repetition rate (1 ms pulse duration) to ensure sufficient film thickness for ex situ characterization. The substrate holder was not heated, allowing the investigation of room-temperature film growth under energetic ion bombardment conditions.

#### 3.3.1 Profilometry

Stylus profilometry was used to measure film thickness by mechanically tracing the surface topography using a diamond-tipped stylus. The technique provides direct measurement of step heights between masked and deposited regions [21], making it particularly useful for verifying film thickness values obtained by QCM.

In profilometry, a stylus with a small tip radius is dragged across the sample surface with a controlled force of 3 mg while its vertical displacement is monitored electromagnetically. The resulting trace provides a profile of the surface from which the step height (film thickness) with vertical resolution down to  $\sim 1$  nm can be extracted.

The Bruker DektakXT stylus profilometer was used in this study. Multiple scans across each step were performed to ensure reproducibility, and the average thickness was calculated from at least three different positions on each sample.

### 3.3.2 X-ray diffraction (XRD)

X-ray diffraction (XRD) was employed to analyze the crystallographic structure of the deposited thin films. XRD is a non-destructive technique that provides detailed information about the crystalline phases present in the material, as well as their lattice parameters, crystallite size, and strain.

Due to the small film thickness, out-of-plane diffraction techniques were used to enhance the film signal relative to the substrate. Two measurement geometries are employed [22]:

- **Symmetrical reflection ( $2\theta/\theta$  scan):** Both incident and diffracted beams make equal angles with the sample surface. This geometry probes lattice planes parallel to the substrate and is suitable for textured films, but substrate peaks can obscure weak film signals.
- **Asymmetrical reflection (thin-film method):** The incident beam is fixed at a small grazing angle  $\alpha$ , while the detector scans in  $2\theta$ . This reduces the X-ray penetration depth from tens of micrometers to a few micrometers, greatly enhancing sensitivity to thin films [22].

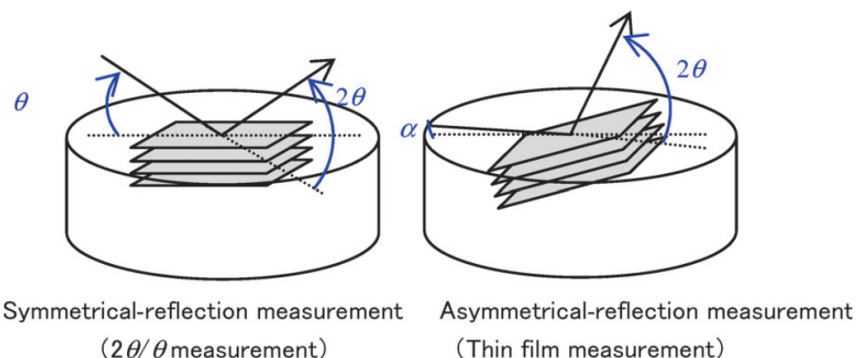


**Figure 3.8.** Schematic of out-of-plane diffraction geometries: symmetrical reflection (left) and asymmetrical reflection (right) for thin film analysis. Taken from [22].

The XRD measurements were performed using a Rigaku Ultima IV system equipped with a non monochromatic  $\text{Cu}_\alpha$  source. The crystallographic structure was determined

by analyzing the diffraction patterns. The Bragg equation used to identify the crystalline phases:

$$2d \sin(\theta) = n\lambda, \quad (3.17)$$

where  $d$  is the spacing between atomic planes,  $\theta$  is the diffraction angle,  $n$  is an integer, and  $\lambda$  is the X-ray wavelength.

### 3.3.3 X-ray reflectivity (XRR)

X-ray reflectometry (XRR) is a non-destructive technique used to determine film thickness, density, and surface or interface roughness by measuring the intensity of X-rays reflected at grazing incidence angles ( $0.01\text{--}5^\circ$ ) [23].

When X-rays strike a flat surface at shallow angles below the critical angle  $\theta_c$ , total external reflection occurs. The critical angle is related to the electron density of the material through:

$$\theta_c = \sqrt{2\delta}, \quad (3.18)$$

where  $\delta$  depends on the material density and composition [23]. Above  $\theta_c$ , X-rays penetrate the film and reflect from interfaces, creating interference patterns known as Kiessig fringes. The period of these oscillations is directly related to film thickness [24]:

$$d \approx \frac{\lambda}{2\Delta\theta}, \quad (3.19)$$

where  $\lambda$  is the X-ray wavelength and  $\Delta\theta$  is the angular spacing between fringes.

The XRR technique provides three key parameters [23]:

- **Film thickness:** Determined from the oscillation period, with accuracy of  $0.1\text{--}0.2$  nm for films in the  $1\text{--}150$  nm range.
- **Density:** Extracted from the critical angle position and oscillation amplitude. Larger density contrast between film and substrate produces higher amplitude oscillations.
- **Surface and interface roughness:** Surface roughness causes faster decay of reflectivity at higher angles, while interface roughness reduces oscillation amplitude.

The measurements were performed using a Rigaku Ultima IV and the measured reflectivity curves were fitted using GlobalFit software, which implements the Parratt recursive formalism [25] to account for multiple reflections at each interface. Film thickness, density, and roughness parameters were refined by fitting the calculated reflectivity curve to the experimental data. Initial thickness estimates from Profilometry

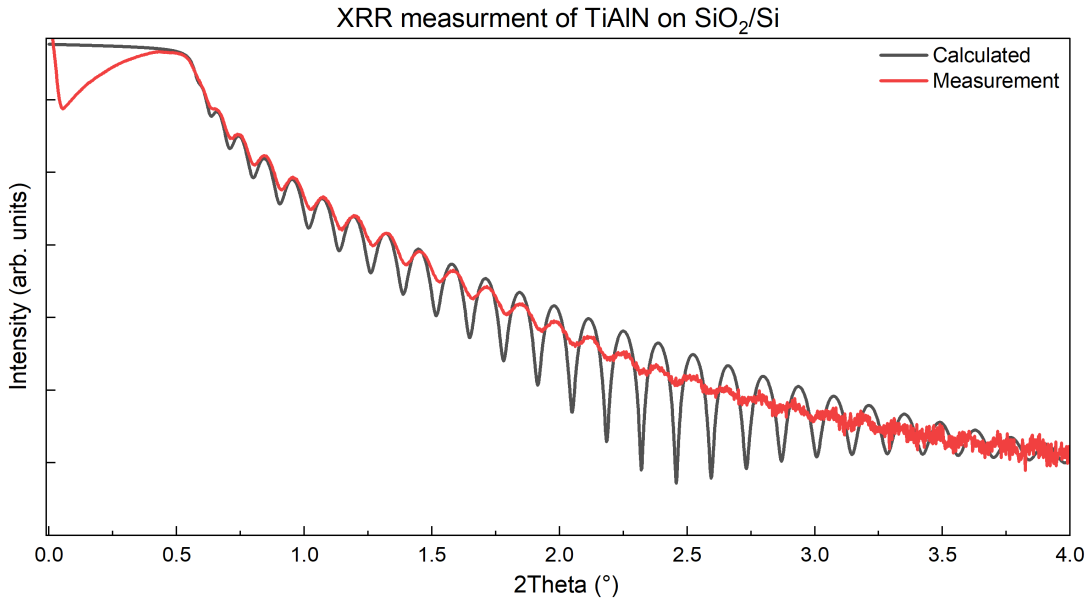


**Figure 3.9.** Example XRR measurement and fit for a TiAlN thin film deposited on Si substrate. The oscillations (Kiessig fringes) arise from interference between reflections from the film surface and the film-substrate interface.

measurements (Section 4.3.1) were used as starting values for the fitting procedure. XRR is particularly suited for verifying thicknesses and characterizing film density and surface roughness for the deposited TiAl and TiAlN films.

### 3.3.4 Scanning electron microscopy (SEM)

Scanning electron microscopy (SEM) was employed to characterize the surface morphology and microstructure of the deposited films. SEM uses a focused electron beam to scan the sample surface, generating secondary electrons (SE) and backscattered electrons (BSE) that provide information about surface topography and compositional contrast, respectively [26, 27].

SEM imaging was performed using a Zeiss Ultra 55 field emission scanning electron microscope equipped with an in-lens detector for high-resolution secondary electron imaging. Samples were imaged at an accelerating voltage of 15 kV with magnifications ranging from 30,000× to 100,000×. The conductive TiAlN films required no additional coating preparation.

The primary objectives of SEM characterization were to:

- Examine surface morphology and the presence of any macroparticles typical of cathodic arc deposition

- Identify microstructural features resulting from different deposition conditions

Representative SEM micrographs and analysis of surface features are presented in Section 4.3.5.

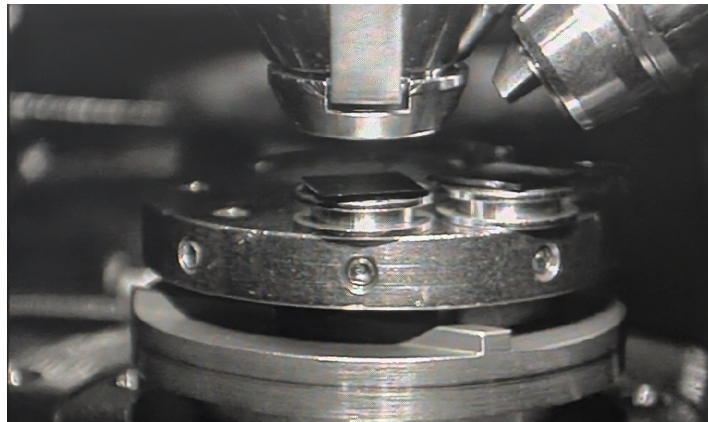


**Figure 3.10.** Interior view as seen by the internal camera of the SEM system during measurements. The chamber with the sample holder stage and detector configuration used for imaging and EDX analysis.

### 3.3.5 Energy-dispersive X-ray spectroscopy (EDX)

Energy-dispersive X-ray spectroscopy (EDX) relies on the ionization of inner-shell electrons by the incident electron beam. When an inner-shell electron is ejected, an electron from a higher energy level fills the vacancy, releasing energy in the form of a characteristic X-ray. The energy of this X-ray is unique to each element, allowing identification and quantification of the sample composition. The intensity of the characteristic X-ray peaks is proportional to the concentration of each element, enabling quantitative analysis through comparison with standards or standardless quantification algorithms [26].

EDX measurements were performed using a silicon drift detector (SDD) integrated with the SEM system, operating at an accelerating voltage of 10 kV. To minimize substrate contribution from the thin films, samples were tilted to 55° relative to the electron beam increasing the effective path length by  $\approx 1.74$ .

Prior to analysis, samples were cleaned ultrasonically in isopropanol to remove loose particles. Organic solvent residues and hydrocarbon contamination from the vacuum system can lead to carbon deposition under electron beam irradiation [26, 27]. A small carbon peak was therefore typically observed in EDX spectra and was excluded from compositional quantification of the TiAlN films. Multiple area measurements were

taken on each sample to verify that all surface features, including any macroparticles or morphological structures, had the same metal-nitride composition as the underlying thin film and to identify potential impurities beyond the surface carbon layer.

The primary elements analyzed were titanium (Ti), aluminum (Al), and nitrogen (N). Oxygen (O), silicon (Si) and carbon (C) were also monitored to assess surface oxidation, contribution from the Si substrate and contamination from isopropanol during the ultrasonic bath cleaning steps. The measured film compositions are used to calculate the effective molar mass  $M_{\text{eff}}$  required for determining total deposited flux from QCM measurements (Section 3.2.4). Compositional results and representative EDX spectra are presented in Section 4.3.4.

## 3.4 Calculation of ion flux and total deposited flux

The plasma diagnostic measurements described in Section 3.2.1–3.2.4 provide ion current, mass flux, and ion energy distributions. To quantify the actual particle arrival rates and relate these to the film, these raw measurements must be converted to particle fluxes (ions, neutrals and activated nitrogen) through the conversion factors and procedures described below. Uncertainty estimates for the calculated fluxes, accounting for instrument uncertainties and measurement statistics, are provided in Appendix A.4.

### 3.4.1 Ion flux from probe and ERMS measurements

The ion flux  $\Gamma_{\text{ion}}$  ( $\text{ions cm}^{-2} \text{s}^{-1}$ ) represents the number of charged metal ions arriving per unit area per unit time. It is calculated from the ion current measured by the Langmuir probe (Section 3.2.1) combined with the mean charge state determined from ERMS measurements (Section 3.2.4):

$$\Gamma_{\text{ion}} = \frac{I_{\text{ion}}}{e\langle Q \rangle A_{\text{probe}}} \quad (3.20)$$

where  $\langle Q \rangle$  is the average charge state determined from ERMS measurements and when available the ratios from EDX measurements,  $e = 1.602 \times 10^{-19} \text{ C}$  is the elementary charge,  $A_{\text{probe}} = 0.196 \text{ cm}^2$  is the probe collection area, and  $R = 400 \Omega$  is the measurement resistor. This combination of probe and mass spectrometer data accounts for the multiply charged nature of the cathodic arc plasma and enables quantitative determination of the particle flux from the electrical current measurement.

$$\langle Q \rangle = \frac{\sum_Q Q \cdot I_Q}{\sum_Q I_Q} \quad (3.21)$$

where  $I_Q$  is the integrated ion current for charge state  $Q$  after applying the mass

transmission correction (Equation 3.10) [28, 5]. This combination of probe and mass spectrometer data accounts for the multiply charged nature of the cathodic arc plasma and enables accurate determination of the particle flux from the electrical current measurement.

### 3.4.2 Total deposited flux from QCM and film characterization

The total deposited flux  $\Phi_{\text{total}}$  (atoms  $\text{cm}^{-2} \text{s}^{-1}$ ) quantifies the arrival rate of all species contributing to film growth, including both ions and neutrals. It is calculated from QCM mass measurements (Section 3.2.2) combined with film composition from EDX (Section 3.3.5):

$$\Phi_{\text{total}} = \frac{\Delta m \cdot N_A}{A_{\text{QCM}} \cdot \Delta t \cdot M_{\text{eff}}} \quad (3.22)$$

where  $\Delta m$  is the mass change measured by QCM over time interval  $\Delta t$ ,  $A_{\text{QCM}} = 1.54 \text{ cm}^2$  is the crystal area (14 mm diameter),  $N_A = 6.022 \times 10^{23} \text{ mol}^{-1}$  is Avogadro's constant, and  $M_{\text{eff}}$  is the effective molar mass calculated from film composition:

$$M_{\text{eff}} = \sum_i x_i M_i = x_{\text{Ti}} \cdot 47.867 + x_{\text{Al}} \cdot 26.982 + x_{\text{N}} \cdot 14.007 \quad (3.23)$$

where  $x_i$  are the atomic fractions from EDX measurements (Table 4.3) and  $M_i$  are the atomic masses.

The effective molar mass of the metallic films is  $M_{\text{eff}} \approx 43.5 \text{ g}\cdot\text{mol}^{-1}$  and for the nitride films:  $M_{\text{eff}} = 31.8\text{--}33.2 \text{ g}\cdot\text{mol}^{-1}$ . ERDA measurements can improve the accuracy of the composition and account for potential impurities in the film [5].

# CHAPTER 4

---

## Results

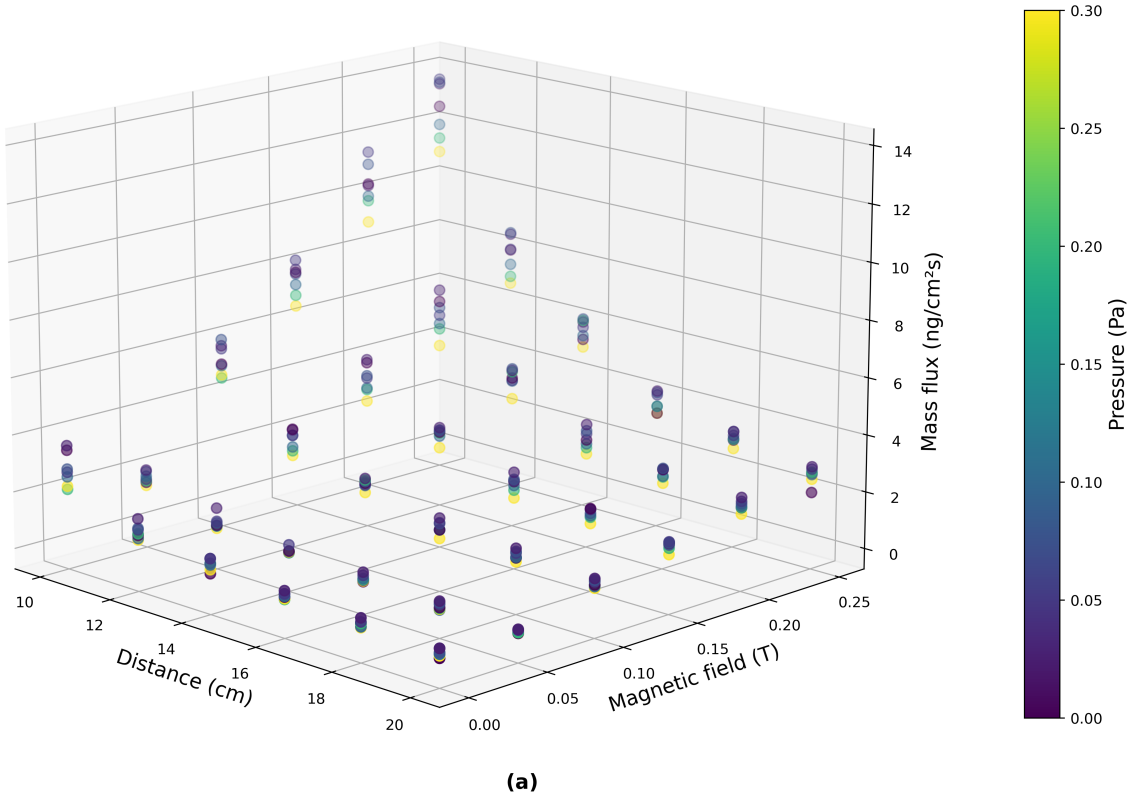
---

### 4.1 Mass deposition rate and ion current measurements

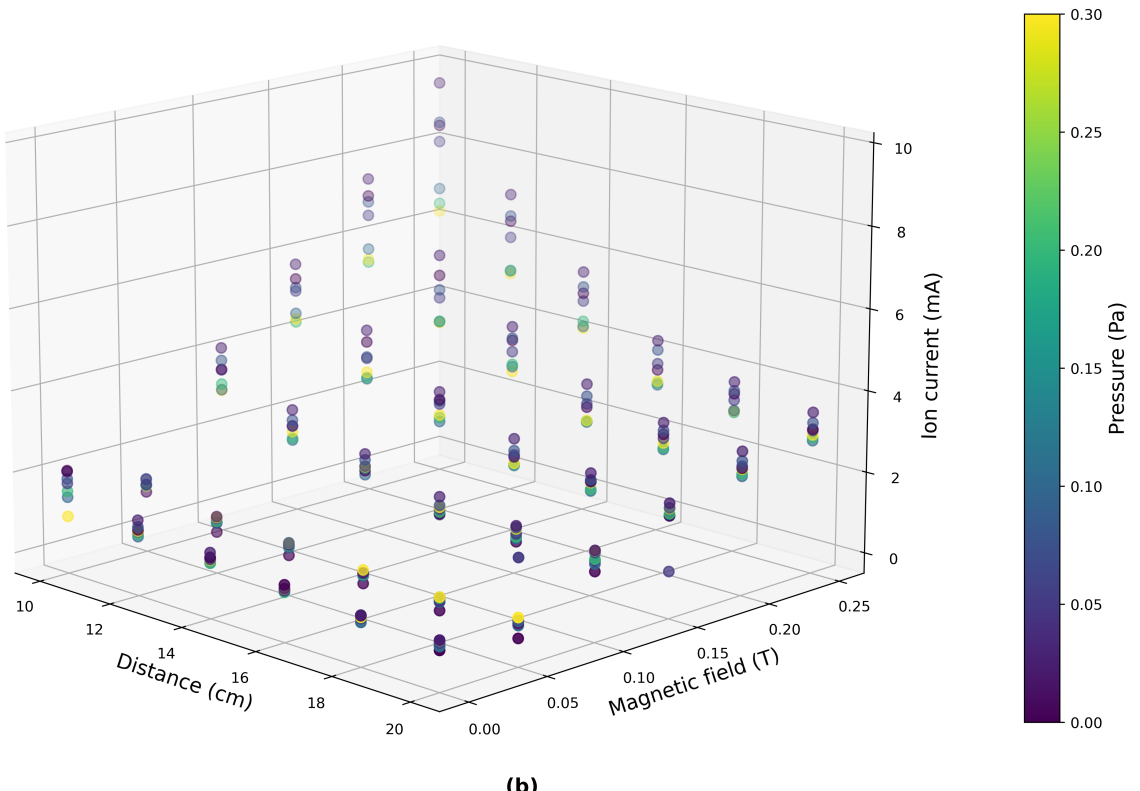
To systematically characterize the plasma dynamics and deposition behavior, measurements were simultaneously conducted using a quartz crystal microbalance (QCM) for mass deposition rate and a biased ion collector probe for ion current density.

The experimental parameter space spanned three variables: distance from the macroparticle filter (from 10 to 20 cm), applied magnetic field strength (from 0 to 0.25 T), and nitrogen background pressure (from 0 to 0.3 Pa), with all permutations measured as listed in Table B.1. At this stage, the raw quantities mass deposition rate (in  $\text{ng cm}^{-2} \text{ s}^{-1}$ ) and ion current (in mA) are shown to establish trends before flux calculations in Section 3.4.

Figure 4.1 provides a three-dimensional visualization of the complete dataset, illustrating how mass deposition rate and ion current vary simultaneously with all three control parameters. Several global trends are immediately apparent: both quantities decrease with increasing distance due to plasma expansion, increase with applied magnetic field due to enhanced plasma. The dependence on nitrogen pressure is more complex and demands detailed investigation.



(a)



(b)

**Figure 4.1.** Three-dimensional visualization of (a) mass flux and (b) ion current as functions of distance (cm), magnetic field strength (T) and nitrogen pressure. Each data point represents an average over 64 pulses at 5 Hz repetition rate, normalized to a single pulse. Surface colors indicate the magnitude of the nitrogen pressure.

To systematically dissect these multidimensional trends, the following subsections examine cross-sections through the parameter space. We begin with the metallic case (no nitrogen, Section 4.1.1) to characterize the plasma behaviour without the reactive gas. The sections 4.1.2–4.1.4 then investigate the individual effects of distance, magnetic field, and nitrogen pressure by varying each parameter with the others constant. The parameter combinations analyzed in detail—distances of 10, 14, and 20 cm; magnetic fields of 0, 0.15, and 0.25 T; and nitrogen pressures of 0.1 and 0.3 Pa—were selected because they correspond to conditions used for energy-resolved mass spectrometry (ERMS) measurements and thin film deposition, enabling direct correlation between plasma diagnostics and film properties in later sections.

#### 4.1.1 Metallic case

In the absence of reactive gas, plasma expansion and deposition dynamics are governed solely by geometric spreading and magnetic enhancement of plasma. Figure 4.2 presents mass deposition rate and ion current as functions of magnetic field strength for three representative distances.

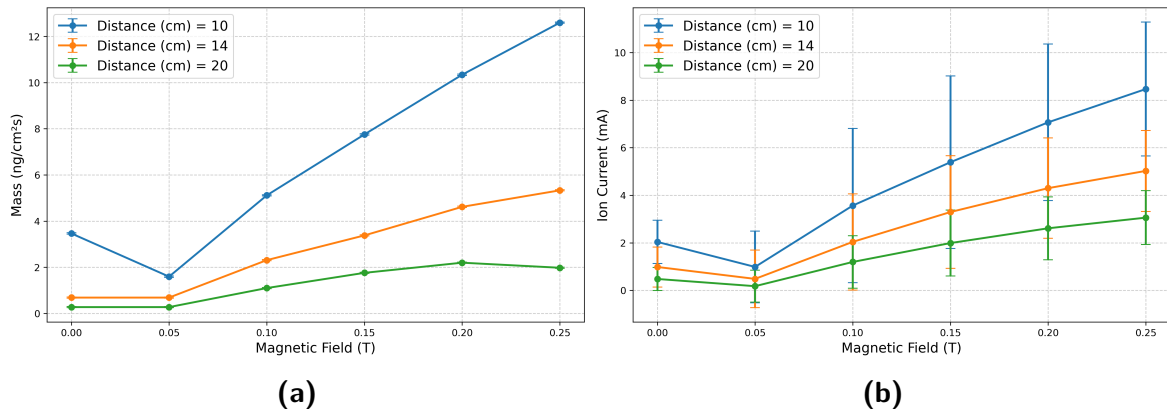


**Figure 4.2.** Magnetic field dependence of (a) mass flux and (b) ion current in metallic mode (0 Pa). Both quantities increase monotonically above 0.1 T due to improved plasma guiding, with the strongest enhancement at 10 cm where radial expansion is minimal. The anomalous dip at 0.05 T (discussed in Sec. 5.2) appears across all distances. Error bars in (a) represent the measurement inaccuracy and in (b) intra-pulse variability.

As shown in Figure 4.2, both mass deposition rate and ion current increase with applied magnetic field. The enhancement is most pronounced at the shortest distance (10 cm), where the magnetic field can effectively guide ions before significant radial expansion occurs. At 20 cm, the plasma has already expanded substantially, reducing the relative impact of magnetic enhancement on the collected flux.

A surprising anomaly appears at 0.05 T, where both quantities drop below their

zero-field values before recovering and increasing at higher fields (0.1 T and above). Similar behavior is observed across all experimental conditions involving increasing magnetic field strength, details of this are discussed in section 5.2.

#### 4.1.2 Measurements as a function of distance

Figure 4.3 reveals the effect of source-to-substrate distance with a constant magnetic enhancement (0.25 T) for both metallic and reactive conditions. Four nitrogen pressures are compared: 0 Pa (metallic), 0.1 Pa, 0.2 Pa, and 0.3 Pa.

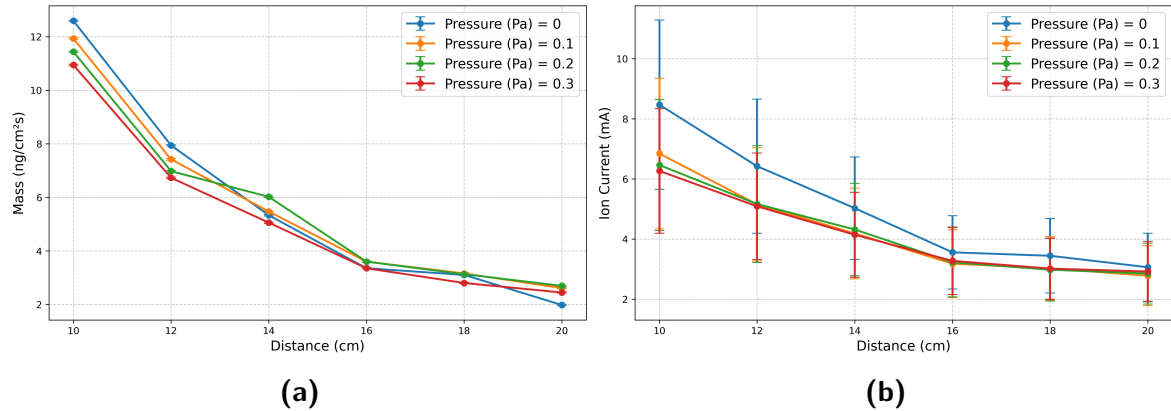


**Figure 4.3.** Distance from the filter exit dependence of (a) mass flux and (b) ion current at 0.25 T magnetic field strength, measured at nitrogen pressures of 0, 0.1, 0.2, and 0.3 Pa.

Both mass deposition rate and ion current decrease with distance, reflecting plasma expansion and the corresponding decrease in plasma density. In metallic mode (0 Pa), mass deposition rate follows an approximate  $1/r^2$  dependence expected for free plasma expansion [3, Chap. 4.3], with 20 cm values approximately 25–30% of those measured at 10 cm.

Ion current exhibits a more pronounced pressure dependence than mass deposition rate. When nitrogen is introduced, the measured current drops steeply, while the QCM mass deposition rate shows more modest changes. The contrast between the two measurements is most pronounced at short distances and diminishes at 14–20 cm.

Additional measurements at constant magnetic field (0 T) and varying distance show similar trends and are presented in Appendix B.2.

#### 4.1.3 Measurements as a function of magnetic field

Figure 4.4 presents mass flux and ion current as a function of magnetic field strength at a fixed intermediate distance (14 cm) for the pressures as in the previous measurements

(metallic, 0.1, 0.2, and 0.3 Pa).

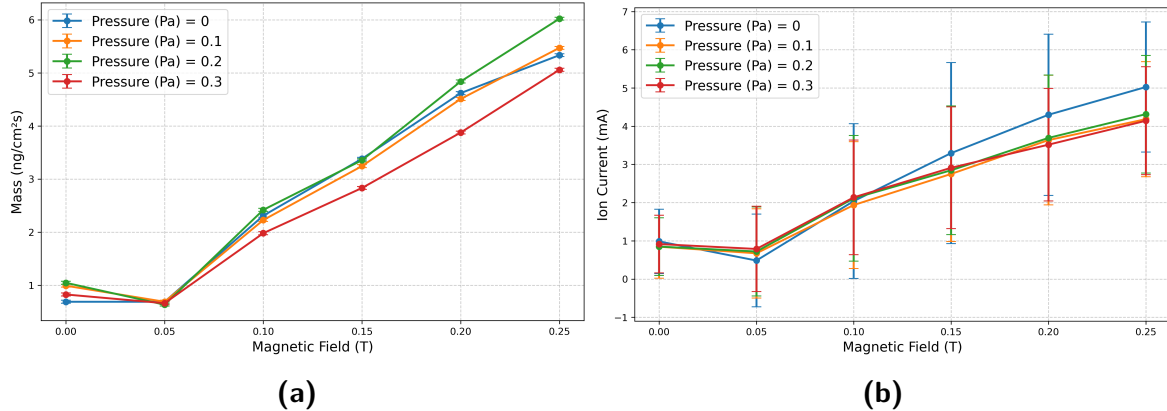


**Figure 4.4.** (a) Mass flux and (b) ion current as functions of magnetic field strength (from 0 to 0.25 T) at 14 cm distance, shown for metallic mode (0 Pa) and reactive mode (0.1, 0.2, 0.3 Pa nitrogen pressure).

The magnetic mirror anomaly at 0.05 T, seen in figure 4.2 previously for 10 cm metallic processes, is slightly visible here at 14 cm but significantly attenuated. Above 0.1 T, both quantities show a clear, consistent increase for all conditions, confirming that magnetic enhancement enhances plasma density and flux at the substrate. The enhancement is approximately linear with field strength in the 0.1–0.25 T range.

Ion current (Figure 4.4b) also increases with magnetic field. At 0.25 T, the ion current in metallic mode (0 Pa) reaches approximately 5 mA, while reactive mode conditions (0.1–0.3 Pa) show currents in the range of 4 mA with substantial error bars. The overlap between metallic and reactive conditions at high fields, combined with the large variation of ion current during a pulse, makes it difficult to draw meaningful conclusions about pressure effects on ion current at 14 cm distance.

To understand the effect of nitrogen pressure more clearly, the next section examines pressure as the primary variable under fixed magnetic field conditions.

#### 4.1.4 Measurements as a function of nitrogen pressure

Figure 4.5 presents mass flux and ion current as functions of nitrogen pressure at maximum magnetic enhancement (0.25 T) for three distances (10, 14, and 20 cm).

At 10 cm, the mass flux exhibits non-monotonic pressure dependence, with a local maximum near 0.05–0.075 Pa before decreasing at higher pressures. The ion current shows substantial scatter across the low pressure ranges suggests that it may be an artifact from the experimental setup. A general decreasing trend is evident despite the scattering.

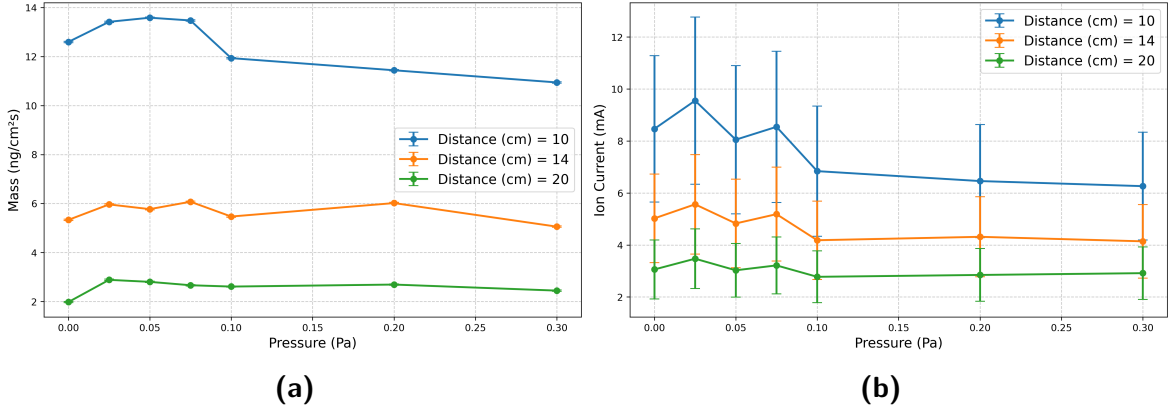


**Figure 4.5.** (a) Mass flux and (b) ion current as functions of nitrogen pressure (0–0.3 Pa) at a magnetic field strength of 0.25 T, shown for the distances 10, 14 and 20 cm.

At 14 cm and 20 cm, both mass deposition rate and ion current become largely independent of nitrogen pressure. Within experimental uncertainty, both quantities remain similar across the 0–0.3 Pa range with the same but weaker scattering at low pressures.

The measurements presented in this section establish the general trends in mass deposition rate and ion current across the experimental parameter space. The apparent trends of increased magnetic field leading to higher mass fluxes and ion currents, larger distances leading to lower mass fluxes and ion currents and a maximum mass flux near the nitrogen pressure of 0.05 Pa. However, these raw quantities do not directly reveal the underlying plasma composition. To address total and ionic fluxes, energy-resolved mass spectrometry was performed under selected conditions to characterize the ion energy distributions and mean charge states, as presented in the following section.

## 4.2 Energy-resolved mass spectrometry results

Energy-resolved mass spectrometry (ERMS) measurements were performed to characterize charge-state distributions and ion energies under selected conditions corresponding to film depositions. The measurements provide charge-state-resolved ion energy distribution functions (IEDFs) for  $\text{Al}^{1+,2+,3+}$ ,  $\text{Ti}^{1+,2+,3+,4+}$  and  $\text{N}/\text{N}_2^{1+}$ , from which mean charge states  $\langle Q \rangle$  (3.21), kinetic energies  $E_{\text{kin}}$  (3.13), and potential energies  $E_{\text{pot}}$  (3.15) are derived. All measurements were performed at 0.25 T magnetic field strength, with particular emphasis on the 14 cm distance selected for systematic film depositions, as well as for all the above mentioned species.

### 4.2.1 Measurements as a function of distance

Figures 4.6 and 4.7 present mean charge states, ion potential energies, and ion kinetic energies as functions of distance for metallic mode (0 Pa) and reactive mode (0.3 Pa N<sub>2</sub>), respectively.

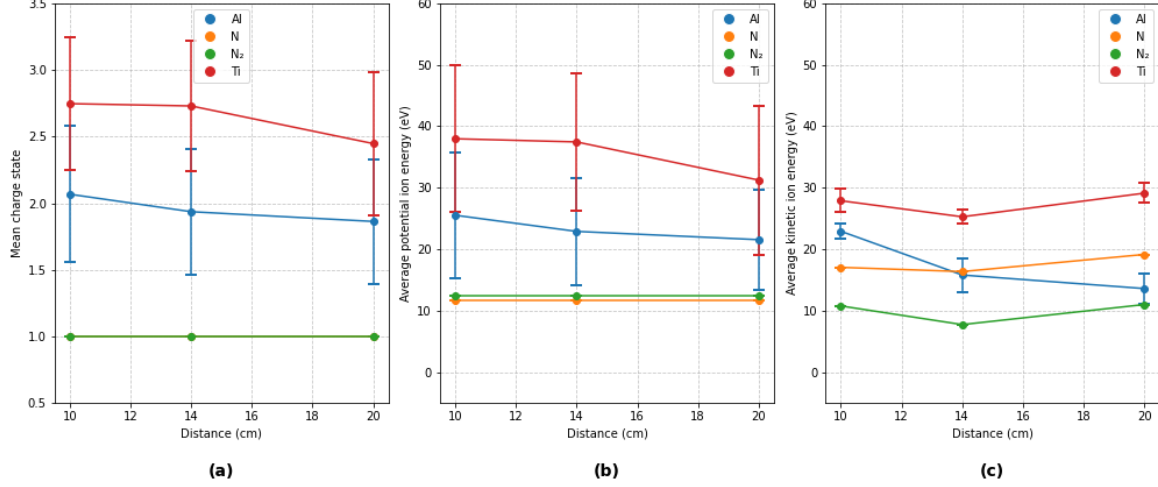


**Figure 4.6.** (a) Mean charge state, (b) average potential energy, and (c) average kinetic energy as functions of distance in metallic mode (0 Pa nitrogen) at 0.25 T magnetic field. Data shown here are for average values of Al, Ti (and N/N<sub>2</sub> measured in all cases) ion species.

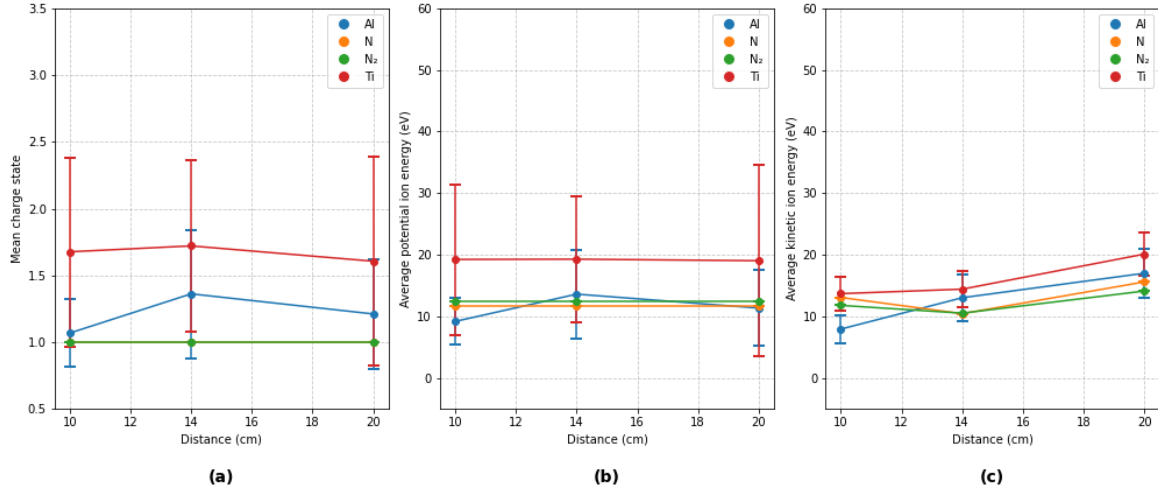


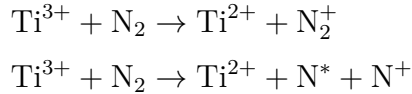
**Figure 4.7.** (a) Mean charge state, (b) average potential energy, and (c) average kinetic energy as functions of distance in metallic 0.3 Pa nitrogen at 0.25 T magnetic field. Data shown here are for average values of Al, Ti and N/N<sub>2</sub> measured ion species.

In metallic mode (Figure 4.6), titanium ions exhibit  $\langle Q \rangle \approx 2.6$  and aluminum ions  $\langle Q \rangle \approx 2.0$  across all distances. These charge states reflect the high electron temperatures ( $T_e \approx 5\text{--}10$  eV) characteristic of cathode spot plasmas [3, Chap. 4.3]. The mean

charge states remain at similar values as a function of distance, varying by less than 10% between 10 and 20 cm, indicating that neutralization is negligible during the travel time through this region on the order of  $\sim 100 \mu\text{s}$  scale.

Potential ion energies depend on the charge state and therefore scale directly with the charge state, with Ti showing  $E_{\text{pot}} \approx 38 \pm 12 \text{ eV}$  at 10 cm decreasing to  $\approx 31 \pm 13 \text{ eV}$  at 20 cm, and Al showing  $E_{\text{pot}} \approx 26 \text{ eV}$  remaining similar across the measurement range. Kinetic energies of the metal ions are in the range of 20–30 eV for both species and remain approximately constant with distance. Importantly, total ion energies ( $E_{\text{kin}} + E_{\text{pot}}$ ) exceed 40 eV at all distances, well above the  $\approx 30 \text{ eV}$  threshold for subplantation-driven densification [11]. This confirms that energetic condensation remains accessible across the entire 10–20 cm range without external heating.

Introducing nitrogen at 0.3 Pa substantially alters the plasma composition (Figure 4.7). Metal ion charge states decrease by up to 50%, coinciding with charge-exchange collisions where multiply charged metal ions interact with nitrogen molecules [7] such as for example:



Potential ion energies decrease from  $\approx 35\text{--}40 \text{ eV}$  (metallic) to  $\approx 20\text{--}30 \text{ eV}$  in reactive mode. Kinetic ion energies show a slight increase in reactive mode. Despite these changes, total ion energies of the metal ions remain in the range of 30 eV at 10 cm. At the 14 cm distance, total metal ion energies are approximately 25–35 eV.

#### 4.2.2 Measurements as a function of pressure

Figures 4.8 and 4.9 present the pressure dependence of charge states and ion energies at 10 cm and 14 cm, respectively. The 14 cm measurements was selected to have a reasonable deposition rate for depositions as well.

At both distances, metal ion charge states generally decrease with increasing nitrogen pressure as charge-exchange collisions accumulate. At 14 cm, the average charge state of Ti decreases from  $\langle Q \rangle \approx 2.7$  (0 Pa) to  $\approx 1.7$  (0.3 Pa), and the one for Al from  $\approx 1.9$  to  $\approx 1.3$ . The overall charge-state reduction is qualitatively similar at both distances with the Al ions showing a negligible increase from 0.2 to 0.3 Pa considering the errorbars.

Kinetic energies show non-monotonic behavior with pressure. At both 10 cm and

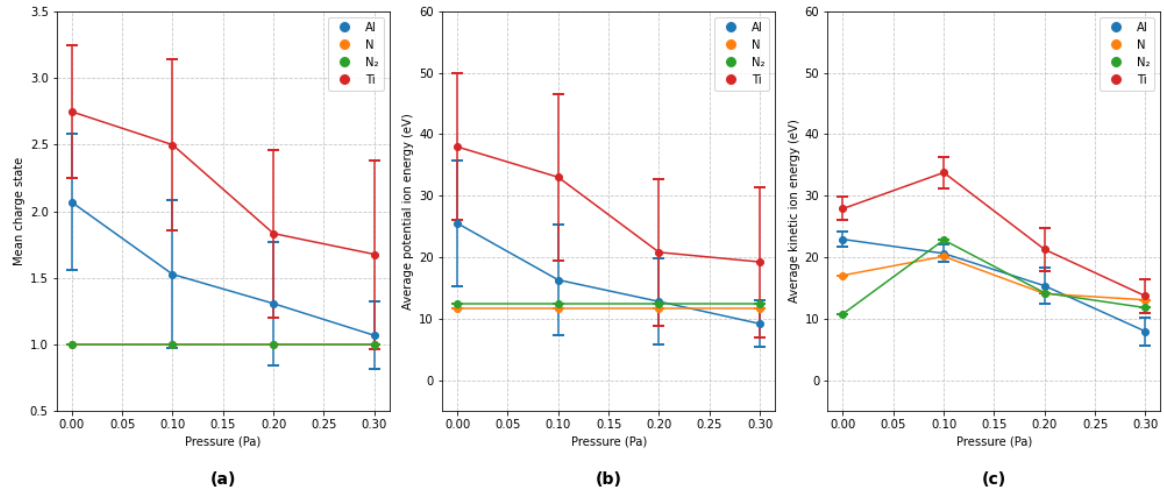


**Figure 4.8.** (a) Mean charge state, (b) average potential ion energy, and (c) average kinetic ion energy as functions of nitrogen pressure for Al, Ti, and N ions at 10 cm distance and 0.25 T magnetic field.

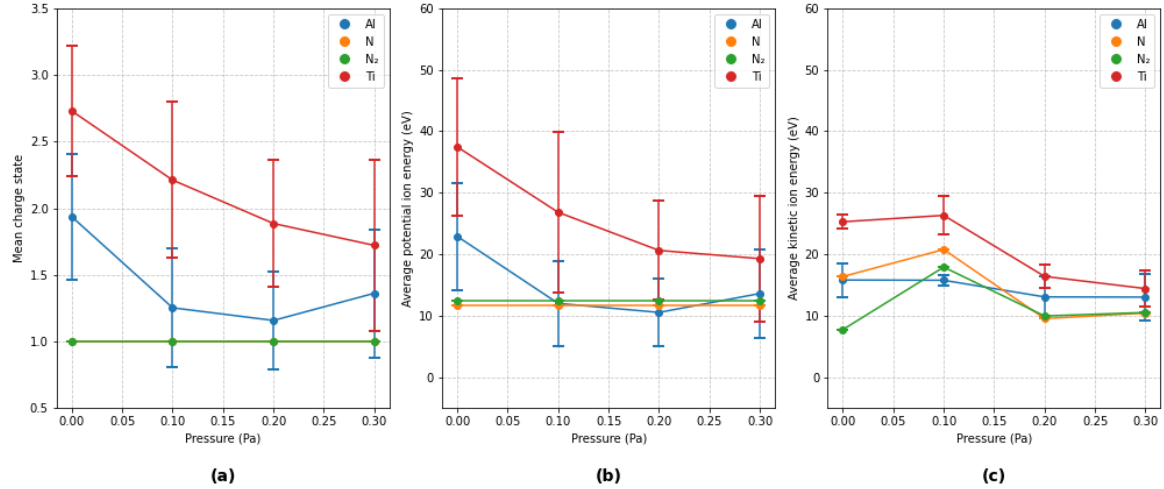


**Figure 4.9.** (a) Mean charge state, (b) average potential ion energy, and (c) average kinetic ion energy as functions of nitrogen pressure for Al, Ti, and N ions at 14 cm distance and 0.25 T magnetic field.

14 cm, Ti and Al exhibit a local maximum near 0.1 Pa, followed by a decrease at higher pressures. The origin of this local maximum is unknown and requires further investigations to understand how nitrogen impacts the plasma at these pressures.

### 4.3 Thin film analysis

Thin films were deposited on Si(100) substrates positioned at 14 cm from the macroparticle filter exit under conditions listed in Table B.1. The substrates were mounted on the substrate holder with the same positions in space used for QCM and ion probe measurements to ensure identical positioning. Films were deposited under four repre-

sentative conditions spanning the parameter space: metallic mode (0 Pa) and reactive mode (0.1, 0.2, 0.3 Pa) at high magnetic field strength (0.25 T). For all depositions the following parameters were used 850 A arc current, 1 ms pulse width, and 5 Hz repetition rate.

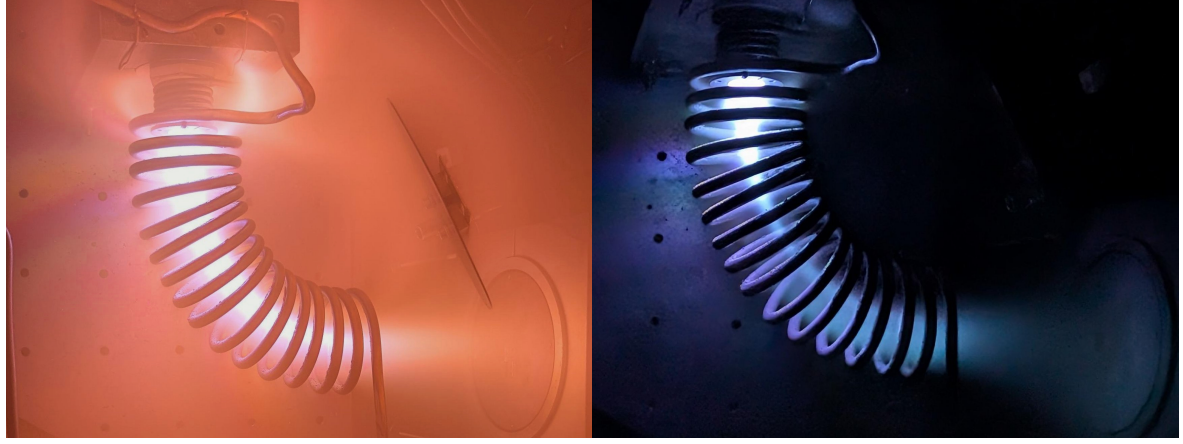


**Figure 4.10.** Photographs of filtered cathodic arc plasma in (a) reactive mode at 0.3 Pa nitrogen pressure and (b) metallic mode. Images are taken during deposition at 14 cm distance with 0.25 T magnetic field. Camera settings: f/1.7, 1/100 s, ISO 90.

### 4.3.1 Profilometry

Profilometry measurements were performed at three positions on each sample: one near the center and one near each edge. The three measurements were averaged to obtain the mean film thickness.

In reactive conditions, the deposition rate was decreased compared to metallic mode. To achieve comparable film thicknesses for characterization, the pulse count was increased from 6000 to 8000 pulses for nitrogen containing depositions. The resulting thickness values are summarized in Table 4.1.

The thickness differences between the QCM and ion probe positions range from 12–30% and were used to correct the final ionic flux values. Films deposited in reactive mode show deposition rates reduced by 30–40% compared to metallic mode, despite the increased pulse count used in subsequent depositions to partially compensate for this reduction.

### 4.3.2 X-ray diffraction (XRD)

X-ray diffraction measurements were performed to characterize the crystallographic structure and degree of crystallinity of the deposited films as a function of nitrogen

**Table 4.1.** Film thickness measured by stylus profilometry at two substrate positions (QCM and ion probe locations) for films deposited at 14 cm distance with 0.25 T magnetic field. All films deposited with 850 A arc current, 1 ms pulses at 5 Hz.

| Film ID | Pressure (Pa) | Pulses | Thickness QCM position (nm) | Thickness Ion-probe position(nm) |
|---------|---------------|--------|-----------------------------|----------------------------------|
| 10      | 0.0           | 6000   | 65                          | 57                               |
| 13      | 0.1           | 8000   | 59                          | 41                               |
| 14      | 0.2           | 8000   | 46                          | 38                               |
| 11      | 0.3           | 8000   | 42                          | 35                               |

pressure. Figure 4.11 shows the diffraction patterns for films deposited at 14 cm distance with 0.25 T magnetic field under varying N<sub>2</sub> pressures from 0 Pa (metallic mode) to 0.3 Pa (reactive mode).

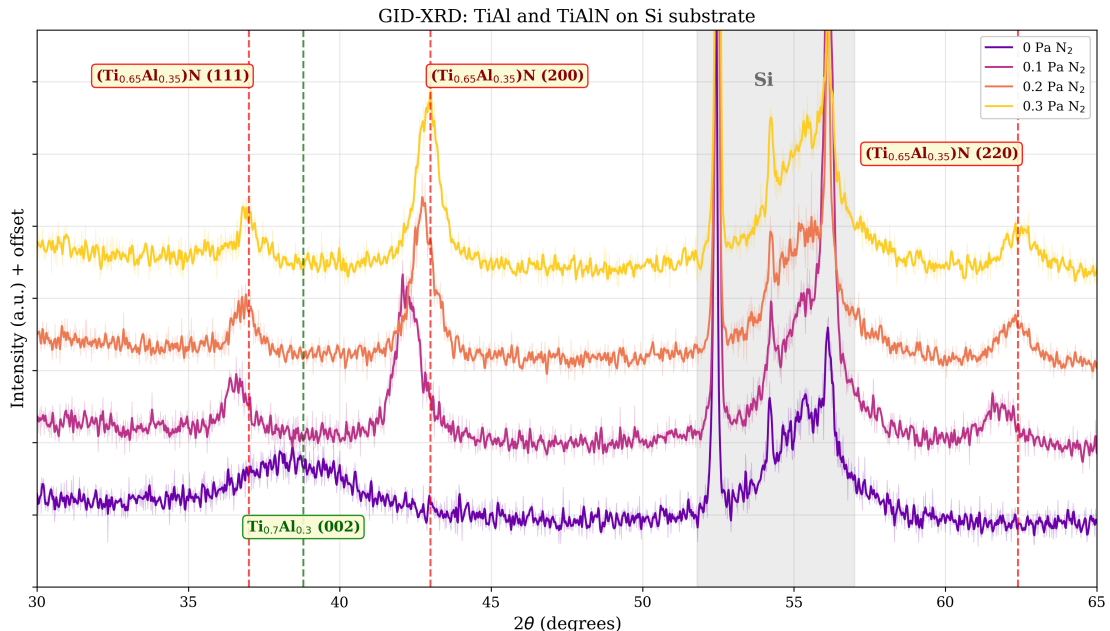


**Figure 4.11.** X-ray diffraction patterns showing hexagonal TiAl phase at 0 Pa and cubic (Ti,Al)N phase at 0.1–0.3 Pa nitrogen pressure. Films deposited at 14 cm with 0.25 T magnetic field. The peaks at 52–57° in the gray shadow area belongs to the Si substrate.

The diffraction patterns reveal a clear transition from metallic to nitride phases with increasing nitrogen pressure:

**Metallic mode (0 Pa N<sub>2</sub>):** At zero nitrogen pressure, the film exhibits a weak, broad peak at approximately 38.8°, consistent with the (002) reflection of hexagonal Ti<sub>0.7</sub>Al<sub>0.3</sub> (space group P6<sub>3</sub>/mmc, PDF 04-004-9157), this material has a similar composition as the cathode material (Ti<sub>0.628</sub>Al<sub>0.372</sub>).

**Reactive mode (0.1–0.3 Pa N<sub>2</sub>):** Introduction of nitrogen alters the film structure. At 0.1 Pa N<sub>2</sub>, three distinct peaks emerge at approximately 37°, 43°, and 62°, corresponding to the (111), (200), and (220) reflections of the cubic B1 (NaCl-type) (Ti<sub>0.65</sub>Al<sub>0.35</sub>)N phase (space group Fm $\bar{3}$ m, PDF 04-017-5094). The hexagonal TiAl peak disappears completely, indicating the nitride phase.

As the nitrogen pressure increases from 0.1 Pa to 0.3 Pa, the peak positions shift progressively closer to the reference values. Small deviations at 0.1 Pa correlate with the lower nitrogen content measured by EDX (33 at.% vs 39 at.%). The reference cubic nitride exhibits a lattice parameter of  $a = 4.202 \text{ \AA}$  and a calculated density of 4.8 g cm<sup>-3</sup> [29], which will be compared with the film densities determined by XRR (Section 4.3.3).

The sharp, well-defined (111), (200), and (220) reflections in all nitride films indicate crystalline growth in Zone T or Zone 1 of Anders' structure zone model [13]. ERMS measurements (Section 4.2) confirmed that ions arriving at the substrate retained energies of 30–50 eV even after transport through the filter and reactive gas environment. These energies exceed the threshold for subplantation and therefore densification [11], enabling room-temperature crystallization through energetic condensation.

### 4.3.3 X-ray reflectometry (XRR)

X-ray reflectometry measurements were performed to determine film thickness and mass density for selected samples. Table 4.2 presents measurements at both substrate positions (QCM and ion current probe locations) for films listed in table 4.2. These measurements provide mass density values and confirm the profilometry measurements.

**Table 4.2.** X-ray reflectivity measurements provide thickness confirmation and mass density values. Mass densities extracted from critical angle and Kiessig fringe spacing are 4.00 g cm<sup>-3</sup> for TiAl and 4.65 to 4.8 g cm<sup>-3</sup> for TiAlN, reaching theoretical bulk density (4.8 g cm<sup>-3</sup>).

| Film ID | Pressure (Pa) | Thickness (nm) |             | Mass density (g/cm <sup>3</sup> )<br>QCM/ion |
|---------|---------------|----------------|-------------|--|
|         |               | QCM            | Ion current |  |
| 10      | 0.0           | 63             | 58          | 4.00   |
| 13      | 0.1           | 46.5           | 38          | 4.80 / 4.75                                  |
| 14      | 0.2           | 42             | 34.5        | 4.80 / 4.75                                  |
| 11      | 0.3           | 45.5           | 39          | 4.65   |

A systematic thickness gradient is observed between the two substrate positions, with the ion current location consistently showing 5–8.5 nm lower thickness compared

to the QCM position, corresponding to a reduction of 8–18%. This spatial non-uniformity is consistent with the profilometry measurements presented in Table 4.1, where thickness differences of 5–18 nm between the two positions were observed across all samples.

The XRR thickness values are on average 10% lower than profilometry measurements. This agreement validates both measurement techniques and confirms that the observed gradient is a real spatial variation in the amount of deposited particles at each measurement device and can therefore be accounted.

The introduction of nitrogen substantially changes the film mass density 4.00 g/cm<sup>3</sup> for metallic films to 4.65–4.80 g/cm<sup>3</sup> for nitride films. This density increase reflects the transition from metallic TiAl to a dense cubic TiAlN nitride phase. The measured densities in reactive mode closely approach the reference value of 4.8 g/cm<sup>3</sup> for stoichiometric cubic (Ti<sub>0.65</sub>Al<sub>0.35</sub>)N [29], confirming crystalline and highly dense cubic thin films.

#### 4.3.4 Energy dispersive X-ray spectroscopy (EDX)

Energy dispersive X-ray spectroscopy was performed to determine the elemental composition of the deposited films as a function of nitrogen pressure. All films were deposited at 14 cm distance with a magnetic field of 0.25 T. Three measurement points were taken on each sample and averaged to obtain representative composition values.

**Table 4.3.** Elemental composition (at.%) determined by EDX measurements and resulting effective molar mass of films deposited at varying nitrogen pressures. Data obtained with averages of up to three positions per sample. All films deposited at 14 cm distance with 0.25 T magnetic field.

| Nitrogen (Pa) | N (at.%) | Al (at.%) | Ti (at.%) | $M_{\text{eff}}$ (g · mol <sup>-1</sup> ) |
|---------------|----------|-----------|-----------|---|
| 0.0           | 0        | 21        | 79        | 43.5                                      |
| 0.1           | 33       | 17        | 50        | 33.2                                      |
| 0.2           | 38       | 15        | 47        | 31.9                                      |
| 0.3           | 39       | 14        | 47        | 31.8                                      |

The results in Table 4.3 reveal several observations:

**Metallic mode (0 Pa):** In metallic film deposition, the film composition shows a Ti:Al ratio of approximately 79:21, which is different to the cathode composition (62.8 at.% Ti; 37.2 at.% Al). The effective molar mass is 43.5 g·mol<sup>-1</sup>, between pure aluminum (27.0 g·mol<sup>-1</sup>) and pure titanium (47.9 g·mol<sup>-1</sup>).

**Reactive mode (0.1–0.3 Pa N<sub>2</sub>):** Nitrogen incorporation reaches approximately 33 at.% at 0.1 Pa and saturates near 39 at.% above 0.2 Pa. The final composition at 0.3 Pa is Ti<sub>0.47</sub>Al<sub>0.14</sub>N<sub>0.39</sub>, close to the reference material composition used for XRD analysis [29]. The deficiency of nitrogen here can potentially be explained by impurities not measurable with EDX and shown by Unutulmazsoy et al.[5]

The effective molar mass is calculated from the atomic fractions  $x_i$  and masses  $M_i$  according to:

$$M_{\text{eff}} = \sum_i x_i M_i = x_{\text{Ti}} \cdot 47.867 + x_{\text{Al}} \cdot 26.982 + x_{\text{N}} \cdot 14.007 \quad (4.1)$$

where the atomic fractions sum to unity ( $x_{\text{Ti}} + x_{\text{Al}} + x_{\text{N}} = 1$ ).

**Effective molar mass trends:** The effective molar mass decreases from 33.2 g·mol<sup>-1</sup> (for 0.1 Pa) to approximately 31.8 g·mol<sup>-1</sup> (for 0.3 Pa), a minor reduction due to higher nitrogen concentration in the thin films.

#### 4.3.5 Scanning electron microscopy (SEM)

Scanning electron microscopy was performed to examine the surface morphology of selected TiAl and TiAlN films. Figure 4.12 shows representative images for films deposited under different conditions.

The metallic TiAl film [Fig. 4.12(a)] exhibits localized surface swelling features, likely resulting from stress relaxation induced by energetic ion bombardment ( $E_{\text{tot}} \approx 60$  eV). Scattered macroparticles are visible as bright spots across the surface, consistent with typical cathodic arc deposition despite magnetic filtering.

The high-magnification image [Fig. 4.12(b)] shows a direct comparison between secondary electron imaging (left, sensitive to topography) and backscattered electron imaging (right, sensitive to atomic number contrast) of the same macroparticle on a TiAlN film. The absence of compositional contrast in the BSE image confirms that the macroparticle has the same elemental composition as the surrounding film, indicating it originated from molten cathode material rather than external contamination.

The reactive TiAlN film [Fig. 4.12(c)] macroparticle are present, but lower quantities than for the metallic case. The overall surface remains relatively smooth between defects.

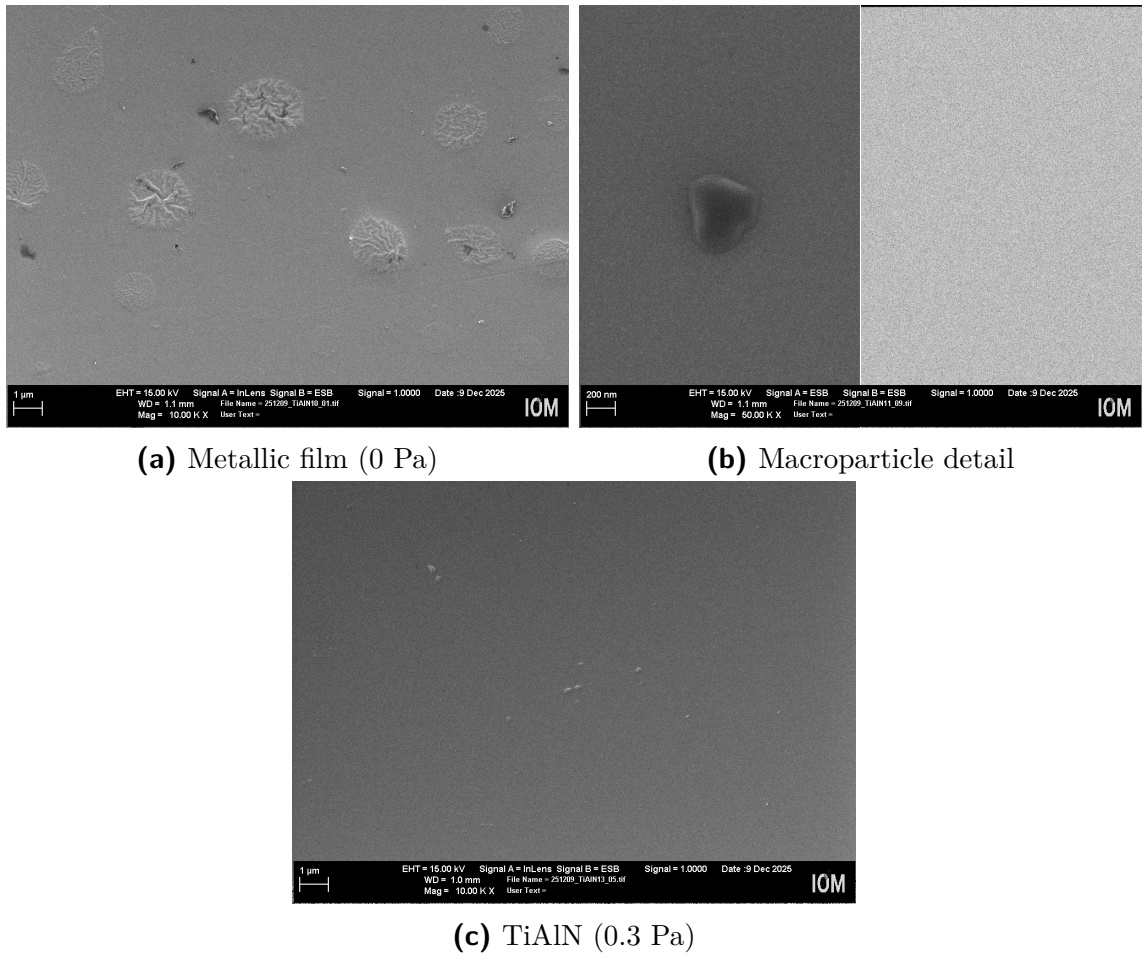


**Figure 4.12.** SEM images of (a) metallic TiAl film, (b) macroparticle on TiAlN film showing secondary electron (left) and backscattered electron (right) imaging at 50,000 $\times$  magnification, and (c) reactive TiAlN film deposited at 0.3 Pa nitrogen pressure. All films deposited at 14 cm distance with 0.25 T magnetic field.

These observations confirm that the magnetic macroparticle filter effectively reduces but does not completely eliminate macroparticle contamination, consistent with the filtered cathodic arc deposition process described in Chapter 3.

## 4.4 Particle flux calculations

The ion current and mass deposition rate measurements contain quantities that must be converted to particle fluxes using charge-state data from ERMS (Section 4.2) and chemical composition data obtained from EDX (Section 4.3.4). This section presents the derived ion flux  $\Gamma_{\text{ion}}$  and total flux  $\Phi_{\text{total}}$  for the 14 cm distances studies.

### 4.4.1 Calculation methods

The ion flux ( $\text{ions}\cdot\text{cm}^{-2}\cdot\text{s}^{-1}$ ) is calculated from the ion current measurements:

$$\Gamma_{\text{ion}} = \frac{I_{\text{ion}}}{e\langle Q \rangle A_{\text{probe}}} \quad (4.2)$$

where  $I_{\text{ion}}$  is the measured ion current,  $e = 1.602 \times 10^{-19} \text{ C}$ ,  $A_{\text{probe}} = 0.196 \text{ cm}^2$ , and  $\langle Q \rangle$  is the weighted mean charge state from ERMS:

$$\langle Q \rangle = \frac{\sum_i Q_i \cdot I_i^{\text{ERMS}}}{\sum_i I_i^{\text{ERMS}}} \quad (4.3)$$

where the sum includes all charge states of Ti and Al.

The total flux ( $\text{atoms}\cdot\text{cm}^{-2}\cdot\text{s}^{-1}$ ) is calculated from QCM measurements:

$$\Phi_{\text{total}} = \frac{\Delta m \cdot N_A}{A_{\text{QCM}} \cdot \Delta t \cdot M_{\text{eff}}} \quad (4.4)$$

where  $\Delta m$  is the mass change over time interval  $\Delta t$ ,  $A_{\text{QCM}} = 1.54 \text{ cm}^2$ ,  $N_A = 6.022 \times 10^{23} \text{ mol}^{-1}$ , and  $M_{\text{eff}}$  is the effective molar mass from Table 4.3.

### 4.4.2 Flux calculations for 14 cm distance studies

Figure 4.13 presents the calculated ion flux and total flux as functions of nitrogen pressure at 14 cm distance with 0.25 T magnetic field.

The ion flux increases monotonically with nitrogen pressure, rising from  $(0.65 \pm 0.2) \times 10^{17} \text{ atoms}\cdot\text{cm}^{-2}\cdot\text{s}^{-1}$  in metallic mode (0 Pa) to  $(0.8 \pm 0.3) \times 10^{17} \text{ atoms}\cdot\text{cm}^{-2}\cdot\text{s}^{-1}$  at 0.1 Pa, and reaching  $(0.95 \pm 0.35) \times 10^{17} \text{ atoms}\cdot\text{cm}^{-2}\cdot\text{s}^{-1}$  at 0.2 Pa before remaining approximately constant at 0.3 Pa. The large error bars (36–72% relative uncertainty, see Table A.1) arise from the combined uncertainties in ion current measurements and ERMS charge-state determination, both dominated by the intrinsic variability of cathodic arc plasmas rather than instrumental limitations. This trend mirrors the ion current behavior shown in Figure 4.5b, where the initial increase from 0 to 0.1 Pa results from additional nitrogen ion production before the flux saturates at higher pressures.

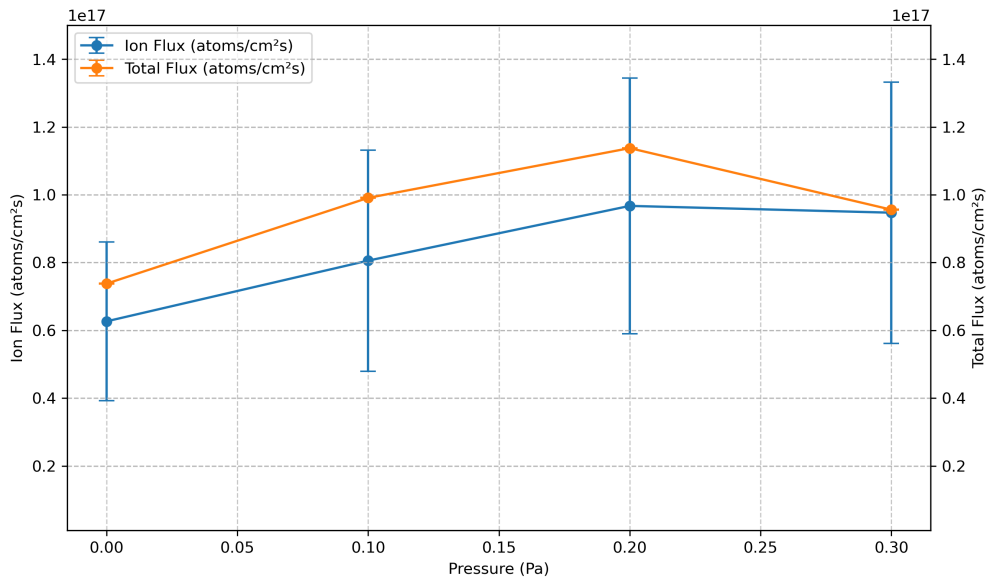


**Figure 4.13.** Ion flux and total flux as functions of nitrogen pressure at 14 cm distance with 0.25 T magnetic field. Error bars represent combined uncertainties from current measurements and charge-state determination (ERMS).

In contrast, the total flux exhibits clear non-monotonic pressure dependence, increasing from  $0.75 \times 10^{17}$  atoms·cm<sup>-2</sup>·s<sup>-1</sup> in metallic mode to a maximum of  $1.15 \times 10^{17}$  atoms·cm<sup>-2</sup>·s<sup>-1</sup> at 0.2 Pa, before decreasing to  $0.95 \times 10^{17}$  atoms·cm<sup>-2</sup>·s<sup>-1</sup> at 0.3 Pa. The QCM-based total flux measurements have uncertainties of approximately 1% (dominated by mass measurement precision), which are smaller than the symbol size in the figure and therefore not visible.

# CHAPTER 5

---

## Discussion and Summary

---

This chapter interprets the experimental findings presented in Chapter 4 and connects them to the theoretical framework established in Chapter 2. The discussion is organized around two central themes, first the film growth mechanisms and then to conclude the plasma transport.

### 5.1 Film Growth and Microstructure

XRD results demonstrate room-temperature crystallization of TiAlN with nitrogen incorporation. The metallic TiAl film (0 Pa) exhibits a broad weak hexagonal reflection, while all reactive mode films (0.1–0.3 Pa nitrogen) develop clearly visible peaks, representing polycrystalline TiAlN (111), (200) and (220) reflections.

XRR measurements show the measured densities are in good agreement with reference values for their respective crystal structures (Table 4.2). The metallic TiAl film shows  $4.00 \text{ g}\cdot\text{cm}^{-3}$ , while TiAlN films reach densities around  $4.65\text{--}4.80 \text{ g}\cdot\text{cm}^{-3}$  in good agreement with the reported theoretical value for cubic TiAlN of  $4.8 \text{ g}\cdot\text{cm}^{-3}$  [29].

EDX measurements show systematic deviations from cathode chemical composition (Table 4.3). In metallic mode, the Ti:Al ratio shifts from 62:37 (cathode) to 79:21 (film), likely arising from differential erosion rates, ionization efficiencies, or transport through the magnetic filter. In reactive mode, the Ti:Al ratio remains similar (77:23) to the metallic films with nitrogen at 39 at.% (0.2–0.3 Pa) not reaching the theoretical concentration of 50 at.%.

XRR and profilometry measurements of the same films show systematic thickness differences (Tables 4.1–4.2), with profilometry yielding slightly higher values for reactive films than XRR measurement. Both techniques reveal 5–8.5 nm gradients between QCM and ion probe positions, attributable to plasma transport through the curved 90 degree magnetic filter. The filter guides electrons along field lines while ions follow electrostatically, causing different species to follow slightly different trajectories and leading to spatial variations in flux and composition [30].

## 5.2 Plasma transport and magnetic field effects

The anomalous decrease in both mass deposition rate and ion current at 0.05 T magnetic field (Figure 4.2) reflects a magnetic mirror effect at the entrance of the EM-coil, where plasma transitions from the weak fringing field (approximately 0.01 T) outside into the stronger field (0.05 T) inside. Electrons with sufficient perpendicular velocity components are reflected, creating a localized space-charge layer that temporarily retards ion flow [3]. At higher fields (0.1 T and above), the beneficial effects of plasma compression and enhanced ionization overcome this mirror loss, restoring monotonic increase. This effect persists across all distances and pressures, indicating it is a fundamental feature of the plasma-coil interaction.

In metallic mode, mass deposition rate follows approximate  $1/r^2$  dependence (Figure 4.3a), consistent with free plasma expansion. Ion current decreases more steeply in reactive mode due to charge-exchange collision and therefore neutralization. The magnetic field enhancement increases both mass flux and ion current by factors of 5 to 8 from zero field to 0.25 T (Figure 4.4), demonstrating effective plasma enhancement.

## 5.3 Reactive mode plasma chemistry

The pressure dependence of mass flux exhibits complex behavior at 10 cm (Figure 4.5b), with an initial decrease from 0 to 0.05 Pa before decreasing at higher pressures. At low nitrogen pressures (0–0.1 Pa), enhanced plasma generation at the cathode from altered spot dynamics and nitrogen ion production contribute to increased measured mass flux. However the ion current show different characteristics, which is gradually decreasing with increasing nitrogen pressure. This is due to the multiple reactions possible with the background gas, for example reduction of the metallic species can lead to ionization, dissociation and excitations.

ERMS measurements confirm this mechanism: mean charge states decrease from  $\langle Q \rangle \approx 2.4$  (metallic) to  $\approx 1.6$  (0.3 Pa reactive), with charge-state distributions shifting

toward lower ionization levels (Figures 4.8–4.9). This represents a 35% reduction in average charge state. Importantly, the total ion energy (kinetic ion energy + potential ion energy) remains above 30 eV across all conditions, sufficient for subplantation processes.

Table 5.1 summarizes the measured plasma parameters and resulting film properties across the pressure range at 14 cm distance with 0.25 T magnetic field.

**Table 5.1.** Plasma parameters and film properties correlation at 14 cm, 0.25 T

| Pressure<br>(Pa) | Ion Flux<br>( $10^{17}$ cm $^{-2}$ s $^{-1}$ ) | Total Flux<br>( $10^{17}$ cm $^{-2}$ s $^{-1}$ ) | $\langle Q \rangle$ | Density<br>(g cm $^{-3}$ ) | XRD Quality            |
|------------------|--|--|---------------------|----------------------------|------------------------|
| 0.0              | 0.6  | 0.75   | 2.4                 | $4.0 \pm 0.1$              | broad hexagonal peak   |
| 0.1              | 0.8  | 1.0  | 2.0                 | $4.8 \pm 0.1$              | sharp phase cubic peak |
| 0.2              | 0.95   | 1.15   | 1.8                 | $4.80 \pm 0.1$             | sharp phase cubic peak |
| 0.3              | 0.95   | 0.95   | 1.6                 | $4.65 \pm 0.1$             | sharp phase cubic peak |

The ionization fraction  $f_{\text{ion}} = \Gamma_{\text{ion}}/\Phi_{\text{total}}$  remains between 0.8 and 1 across all pressures. This high ionization persists even as mean charge states decrease by 35% from metallic to reactive mode, confirming that charge-exchange reduces individual ion charges without substantial neutralization of the metal plasma. In reactive mode, the ionization fraction additionally benefits from activated (ionized and otherwise excited) nitrogen species generated through plasma-gas interactions, contributing to the measured ion flux while the metal plasma itself remains highly ionized.

Total flux exhibits non-monotonic pressure dependence with maximum at 0.2 Pa (54% increase over metallic mode), while ion flux remains approximately constant. This indicates that reactive film formation enhances mass deposition through incorporation of nitrogen atoms from the gas phase, while the metal ion flux remains determined primarily by arc current and magnetic field. The total flux decrease at 0.3 Pa is unknown and needs further investigation to clarify.

### 5.3.1 Activated nitrogen species

EDX measurements (Table 4.3) show substantial nitrogen incorporation in reactively deposited films (33–39 at.%), while ERMS measurements detect weaker N $^+$ /N $_2^+$  signals (10–28 at.%) compared to the total nitrogen in films. The imbalance suggests that nitrogen has some excited species but since ERMS estimates the nitrogen contents via the overall species counts, the imbalance can only be used as a hint towards activated nitrogen.

## 5.4 Summary and Conclusions

This thesis addressed the challenge of understanding ion flux and energy effects in room-temperature TiAlN film growth via filtered cathodic arc deposition. While previous work on (V,Al)N demonstrated that magnetic fields enhance both ion charge states and ion flux simultaneously [5, 6], the individual role of ion flux as an independent variable remained unresolved. This work extended that framework to the industrially relevant TiAlN system by combining QCM and ion probe measurements with ERMS charge-state analysis and film characterization (XRD, XRR, EDX, SEM and Profilometry). Measurements across varying magnetic field strength (0–0.25 T), nitrogen pressure (0–0.3 Pa), and spatial position (10–20 cm) enabled quantification of ion and atomic fluxes while distinguishing contributions from ionized versus neutral nitrogen species.

The methodology revealed nearly full ionization fractions across all conditions, demonstrating the dominant role of ions in thin film deposition. High magnetic fields increased both mass flux and ion current, while charge-exchange collisions in reactive mode reduced mean charge states by 35% without proportionally decreasing ion flux. Film analysis confirmed that ion energies exceeding 30 eV enable room-temperature crystallization of dense cubic TiAlN films.

## 5.5 Outlook

Further work should focus on characterizing neutral species contributions to identify potential gaps in the flux balance. Improved measurement stability with more consistent ion currents would help to resolve subtle trends obscured by current error bars. Systematic investigation of pressure-dependent sticking coefficients is needed to explain the flux behavior at higher pressures. A potential material for those investigations can be TiN as a simpler binary system before extending to multi-component materials like TiAlN.

More accurate film composition measurements using Elastic Recoil Detection Analysis (ERDA) would reduce uncertainties in the effective molar mass  $M_{\text{eff}}$  and improve the precision of total flux calculations. ERDA provides direct quantification of light elements like nitrogen without the matrix absorption effects that limit EDX accuracy, potentially revealing systematic compositional trends that are currently obscured by measurement uncertainty.

# CHAPTER 6

---

## Acknowledgments

---

In this last part I want to express my sincere thanks to all the people that helped, assisted and guided me for this project.

First of all I would like to thank my supervisor Prof. Dr. Benjamin Dietzek-Ivanšić whose attention to detail and ability to ask the right questions at critical moments significantly improved the quality of this research. Furthermore all the people of the plasma group at IOM and especially high praise has to be given to Dr. Dmitry Kalanov, who was there for every issue and every success always looking for a solution and deduction, acting like a mentor. Additionally he is such a warm and friendly colleague just like the next person, who I want to lay out my gratitude towards: Dr. Yeliz Unutulmazsoy believed in me from the beginning and did everything imaginable to make life at IOM easy and enjoyable. Subsequently I want to thank Ramadan Saleh and Uwe Gey with which I spent a lot of fun and quality time in the laboratory keeping the atmosphere light and productive. Furthermore I want to thank Jens Bauer who with his excellent expertise could provide me with EDX/SEM data for very thin films.

Secondly I want to thank my amazing friend group; including Visar who introduced me to IOM (and hopefully more ;-P); my roommates Xuewei and Tom who motivated me with loads of cuppa and food ; Berta for an awesome arm sleeve tattoo and hopefully the next part this year; Kylian, Vincenz and Oliver who were always there for the mandatory Counterstrike tilt; I want single out Dennis DJ NETTO whose music motivated me through the hard days and is just straight fire; Chandramouli and Thiagarajan for introducing me to amazing dishes and providing true friendship; and finally Visar who is always there to go eat Toscka at Syrian bistro.

Thirdly I want to thank my supporting family for always being there for me in all moments of life. In keiner besonderen Reihenfolge sondern nur wie es mir gerade eingefallen ist: Anne als unser Dungeon Meister, was mit Theo und mir bestimmt nicht leicht ist und auch immer schwerer wird, Msma die immer an meinen Fortschritt interessiert ist und mich sogar im Labor besucht hat, Papa der mich an manchen Stellen vielleicht sogar zu viel preist und alle anderen Familienmitglieder, die mir stets ein Gefühl der Wertschätzung vermitteln.

Fourthly I want to thank a few things which just make life better, Sox your scratches keep my arm and hands always scared but your purring makes it all worth it. My childhood obsession of star trek, which got me interested in science, the world and society, combating stereotypes and prejudice making me the man I am today. Finally websites like Jetpunk, Sporkle and Geoguessr, which always spark my need to learn more about Geography, History and General Knowledge.

---

## Bibliography

---

- [1] S. Paldey and S. C. Deevi. “Single layer and multilayer wear resistant coatings of (Ti,Al)N: a review”. In: *Materials Science and Engineering: A* 342.1–2 (2003), pp. 58–79. DOI: [10.1016/S0921-5093\(02\)00259-9](https://doi.org/10.1016/S0921-5093(02)00259-9).
- [2] P. H. Mayrhofer, D. Music, and J. M. Schneider. “Ab initio calculated binodal and spinodal of cubic  $Ti_{1-x}Al_xN$ ”. In: *Applied Physics Letters* 88.7 (2006), p. 071922. DOI: [10.1063/1.2177360](https://doi.org/10.1063/1.2177360).
- [3] André Anders. *Cathodic arcs: from fractal spots to energetic condensation*. Vol. 50. Springer, 2008.
- [4] André Anders and George Yu Yushkov. “Ion flux from vacuum arc cathode spots in the absence and presence of a magnetic field”. In: *Journal of Applied Physics* 91.8 (2002), pp. 4824–4832. ISSN: 0021-8979.
- [5] Yeliz Unutulmazsoy et al. “Toward decoupling the effects of kinetic and potential ion energies: Ion flux dependent structural properties of thin (V,Al)N films deposited by pulsed filtered cathodic arc”. In: *Journal of Vacuum Science & Technology A* 41.6 (2023). ISSN: 0734-2101. DOI: [10.1116/6.0002927](https://doi.org/10.1116/6.0002927). URL: <https://doi.org/10.1116/6.0002927>.
- [6] Dmitry Kalanov et al. “Decoupling the effects of potential energy, kinetic energy, and ion flux on crystallinity of V-Al and V-Al-N thin films in pulsed filtered cathodic arc deposition”. In: *Surface and Coatings Technology* 497 (2025). ISSN: 02578972. DOI: [10.1016/j.surfcoat.2024.131720](https://doi.org/10.1016/j.surfcoat.2024.131720).
- [7] J. Benedikt and A. Kersten H. and Henning. “Quadrupole mass spectrometry of reactive plasmas”. In: *Journal of Physics D: Applied Physics* 40.20 (2007), pp. 6300–6316. DOI: [10.1088/0022-3727/40/20/S13](https://doi.org/10.1088/0022-3727/40/20/S13).

- [8] Soheil Karimi Aghda et al. “Ion kinetic energy- and ion flux-dependent mechanical properties and thermal stability of (Ti,Al)N thin films”. In: *Acta Materialia* 251 (2023), p. 118897. DOI: [10.1016/j.actamat.2023.118897](https://doi.org/10.1016/j.actamat.2023.118897).
- [9] G. A. Mesyats. “Ecton mechanism of the vacuum arc cathode spot”. In: *IEEE Transactions on Plasma Science* 23.6 (1995), pp. 879–883. DOI: [10.1109/27.476469](https://doi.org/10.1109/27.476469).
- [10] Burkhard Jüttner. “Cathode spots of electric arcs”. In: *Journal of Physics D: Applied Physics* 34.17 (2001), R103–R123. DOI: [10.1088/0022-3727/34/17/202](https://doi.org/10.1088/0022-3727/34/17/202).
- [11] Y. Lifshitz et al. “Subplantation model for film growth from hyperthermal species”. In: *Physical Review B* 41.15 (1990), pp. 10468–10480.
- [12] John A. Thornton. “High rate thick film growth”. In: *Annual Review of Materials Science* 7 (1977), pp. 239–260. DOI: [10.1146/annurev.ms.07.080177.001323](https://doi.org/10.1146/annurev.ms.07.080177.001323).
- [13] André Anders. “A structure zone diagram including plasma-based deposition and ion etching”. In: *Thin Solid Films* 518.15 (2010), pp. 4087–4090. DOI: [10.1016/j.tsf.2009.10.145](https://doi.org/10.1016/j.tsf.2009.10.145).
- [14] R. Rachbauer et al. “Decomposition pathways in age hardening of Ti-Al-N films”. In: *Journal of Applied Physics* 110.2 (2011), p. 023515. DOI: [10.1063/1.3610451](https://doi.org/10.1063/1.3610451).
- [15] Francis F. Chen. *Introduction to Plasma Physics and Controlled Fusion*. Vol. 1. New York: Springer, 1984. ISBN: 978-0-306-41332-2.
- [16] Günter Sauerbrey. “Verwendung von Schwingquarzen zur Wägung dünner Schichten und zur Mikrowägung”. In: *Zeitschrift für Physik* 155.2 (Apr. 1959), pp. 206–222. DOI: [10.1007/bf01337937](https://doi.org/10.1007/bf01337937).
- [17] *EQP Technical Manual: Energy-Resolving Quadrupole Mass Spectrometer*. Hiden Analytical. Warrington, UK, 2024. URL: <https://www.hidenanalytical.com>.
- [18] P. H. Dawson. *Quadrupole Mass Spectrometry and Its Applications*. Chichester, UK: IM Publications, 1997. ISBN: 978-1-901019-01-4.
- [19] R. E. March and R. J. Hughes. *Quadrupole Storage Mass Spectrometry*. Wiley, 1989. ISBN: 978-0-471-85841-0.
- [20] Hiden Analytical. *EQP: Mass and Energy Analyser for plasma diagnostics*. [https://www.hidenanalytical.com/wp-content/uploads/2016/08/EQP-poster\\_A1\\_print.pdf](https://www.hidenanalytical.com/wp-content/uploads/2016/08/EQP-poster_A1_print.pdf). [Accessed 18-11-2025]. 2016.
- [21] C. Y. Poon and B. Bhushan. *Comparison of surface roughness measurements by stylus profiler, AFM and non-contact optical profiler*. Vol. 190. 1. 1995, pp. 76–88. DOI: [10.1016/0043-1648\(95\)06697-7](https://doi.org/10.1016/0043-1648(95)06697-7).
- [22] Toru Mitsunaga. “X-ray thin-film measurement techniques II. Out-of-plane diffraction measurements”. In: *The Rigaku Journal* 25.1 (2009), pp. 7–12.

- [23] Miho Yasaka. “X-ray thin-film measurement techniques: V. X-ray reflectivity measurement”. In: *The Rigaku Journal* 26.2 (2010), pp. 1–9.
- [24] H. Kiessig. “Interferenz von Röntgenstrahlen an dünnen Schichten”. In: *Annalen der Physik* 402.7 (1931), pp. 769–788. DOI: [10.1002/andp.19314020702](https://doi.org/10.1002/andp.19314020702).
- [25] L. G. Parratt. “Surface Studies of Solids by Total Reflection of X-Rays”. In: *Physical Review* 95.2 (1954), pp. 359–369. DOI: [10.1103/PhysRev.95.359](https://doi.org/10.1103/PhysRev.95.359).
- [26] Joseph I. Goldstein et al. *Scanning Electron Microscopy and X-Ray Microanalysis*. 4th. New York: Springer, 2017. DOI: [10.1007/978-1-4939-6676-9](https://doi.org/10.1007/978-1-4939-6676-9).
- [27] Ludwig Reimer. *Scanning Electron Microscopy: Physics of Image Formation and Microanalysis*. 2nd. Vol. 45. Springer Series in Optical Sciences. Berlin: Springer, 1998. DOI: [10.1007/978-3-540-38967-5](https://doi.org/10.1007/978-3-540-38967-5).
- [28] Robert Franz, Peter Polcik, and André Anders. “Ion Charge State Distributions of Al and Cr in Cathodic Arc Plasmas from Composite Cathodes in Vacuum, Argon, Nitrogen, and Oxygen”. In: *IEEE Transactions on Plasma Science (manuscript number: TPS6186. R1)* (2013).
- [29] International Centre for Diffraction Data. *Aluminum Titanium Nitride, Ti<sub>0.65</sub>Al<sub>0.35</sub>N*. PDF Card No. 04-017-5094, ICDD Database. Crystal structure data: Space group Fm $\bar{3}$ m (225),  $a = 4.202(9)$  Å, calculated density 4.885 g/cm<sup>3</sup>. Based on X-ray absorption study by Gago et al., *J. Appl. Phys.* 105 (2009). 2013.
- [30] M. M. M. Bilek, Y. Yin, and D. R. McKenzie. “A study of filter transport mechanisms in filtered cathodic vacuum arcs”. In: *IEEE Transactions on Plasma Science* 24.3 (1996), pp. 1165–1173. DOI: [10.1109/27.533126](https://doi.org/10.1109/27.533126).
- [31] R. E. Miller and D. I. Bolef. “Shear modulus and internal friction in single-crystal quartz at low temperatures”. In: *Journal of Applied Physics* 39.11 (1968), pp. 5815–5821. DOI: [10.1063/1.1656042](https://doi.org/10.1063/1.1656042).
- [32] C. Lu and O. Lewis. “Investigation of film-thickness determination by oscillating quartz resonators with large mass load”. In: *Journal of Applied Physics* 43.11 (1972), pp. 4385–4390. DOI: [10.1063/1.1660985](https://doi.org/10.1063/1.1660985).
- [33] *SQM-160 Multi-Film Rate/Thickness Monitor Operating Manual*. PN 074-511-P1E. INFICON. Bad Ragaz, Switzerland, 2015. URL: <https://www.inficon.com>.

---

## List of Figures

---

|  |    |
|--|----|
| 2.1 Schematic of cathode spot operation . . . . .                          | 11 |
| 2.2 Structure-zone diagram for plasma based thin film deposition . . . . . | 18 |
| 3.1 Pulse waveforms for arc and EM-coil . . . . .                          | 22 |
| 3.2 Vacuum chamber setup with diagnostics . . . . .                        | 23 |
| 3.3 Ion collector probe construction . . . . .                             | 24 |
| 3.4 Ion probe circuit diagram . . . . .                                    | 24 |
| 3.5 Voltage waveform across the shunt resistor . . . . .                   | 25 |
| 3.6 QCM sensor assembly . . . . .  | 26 |
| 3.7 ERMS schematic diagram . . . . .                                       | 28 |
| 3.8 Schematic of diffraction geometries for XRD . . . . .                  | 32 |
| 3.9 Example XRR measurement and fit . . . . .                              | 34 |
| 3.10 Interior view of the SEM sample chamber . . . . .                     | 35 |
| 4.1 3D visualization of mass flux and ion current . . . . .                | 39 |
| 4.2 Metallic mode measurements vs. magnetic field . . . . .                | 40 |
| 4.3 Mass and ion current vs. distance . . . . .                            | 41 |
| 4.4 Mass and ion current vs. magnetic field . . . . .                      | 42 |
| 4.5 Mass and ion current vs. nitrogen pressure . . . . .                   | 43 |
| 4.6 ERMS measurements in metallic mode . . . . .                           | 44 |
| 4.7 ERMS measurements in reactive mode . . . . .                           | 44 |
| 4.8 ERMS measurements at 10 cm . . . . .                                   | 46 |
| 4.9 ERMS measurements at 14 cm . . . . .                                   | 46 |
| 4.10 Plasma plume photographs . . . . .                                    | 47 |
| 4.11 XRD patterns for varying nitrogen pressure . . . . .                  | 48 |
| 4.12 SEM surface morphology . . . . .                                      | 52 |
| 4.13 Ion and total flux vs. pressure . . . . .                             | 54 |

|     |   |    |
|-----|---|----|
| A.1 | Holder assembly for plasma diagnostics . . . . .                          | 67 |
| A.2 | Charge-state-resolved ion energy distribution functions for Ti . . . . .  | 68 |
| A.3 | Charge-state-resolved ion energy distribution functions for Al . . . . .  | 68 |
| A.4 | Example ion current waveform showing variability within a pulse . . . . . | 71 |
| A.5 | Ion current probe biasing tests . . . . .                                 | 75 |
| A.6 | Pulse to pulse variation of mean ion current . . . . .                    | 76 |
| B.1 | Pulse waveform at 100 V input . . . . .                                   | 77 |
| B.2 | Additional distance measurements . . . . .                                | 78 |
| B.3 | Magnetic field correlation with charge state . . . . .                    | 78 |

---

## List of Tables

---

|     |  |    |
|-----|--|----|
| 2.1 | Characteristic ion properties for Ti and Al . . . . .                  | 13 |
| 3.1 | Mass-to-charge ratios for ion species . . . . .                        | 29 |
| 4.1 | Profilometry film thickness measurements . . . . .                     | 48 |
| 4.2 | XRR derived thickness . . . . .  | 49 |
| 4.3 | Film composition from EDX . . . . .                                    | 50 |
| 5.1 | Plasma parameters and film properties correlation at 14 cm, 0.25 T . . | 57 |
| A.1 | Summary of measurement uncertainties . . . . .                         | 73 |
| A.2 | Summary of pulse measurement statistics . . . . .                      | 76 |
| B.1 | Complete overview of experimental measurements . . . . .               | 79 |

# APPENDIX A

---

## Experimental Methods supplementary

---

### A.1 Longer QCM depositions

For larger mass loadings of the QCM, the linear approximation fails and the Z-match™ technique is used. This method, introduced by Lu and Lewis in 1972 on the basis of Miller and Bolef's theoretical treatment [31, 32], incorporates the acoustic properties of both the quartz and the deposited film via the acoustic impedance ratio

$$Z = \left( \frac{d_q \mu_q}{d_f \mu_f} \right)^{1/2}, \quad (\text{A.1})$$

with  $d$  and  $\mu$  denoting the density and shear modulus of quartz ( $q$ ) and film ( $f$ ), respectively [33]. In practice, the controller applies a correction function  $f(Z)$  to the Sauerbrey relation,

$$m_f = \frac{N_{\text{AT}} d_q \pi r^2}{F_q^2} \cdot \Delta F \cdot f(Z), \quad (\text{A.2})$$

which compensates for the acoustic mismatch and extends the validity of thickness determination up to  $\sim 0.4F_q$ .

### A.2 Holder assembly design

The integrated holder assembly (Figure A.1) enabled simultaneous QCM and ion probe measurements with minimal spatial separation. The aluminum mount positioned both diagnostics as close as practicable to bring the flux and plasma conditions as close as

possible between measurement locations.

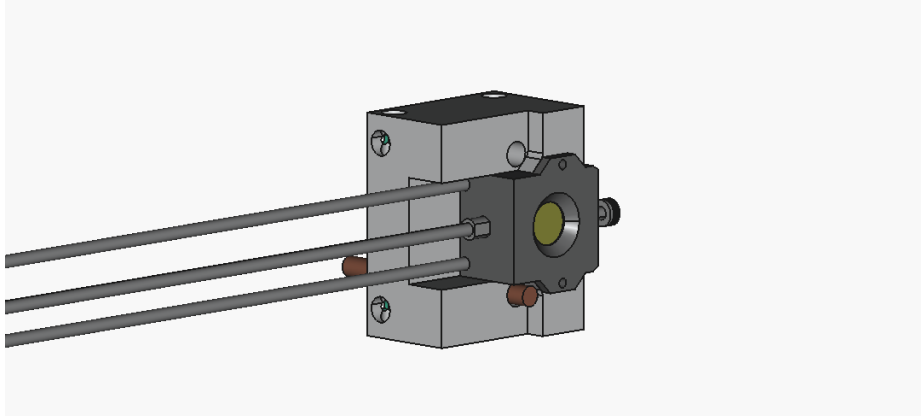


**Figure A.1.** Holder assembly for In-Situ plasma Diagnostics: Integrated QCMs and Ion Collector Probe (interactive 3D model; static preview shown in non-Adobe viewers).

## A.3 Data processing workflow

Experimental data were processed using custom Python scripts to ensure consistency and reproducibility across all measurements. This section describes the data handling procedures and processing workflows used throughout this work.

### A.3.1 Data organization and logbook system

A central Excel logbook served as the reference for all measurements, with each measurement identified by a unique suffix and linked to its corresponding data files. The logbook recorded:

- Date and time of measurement
- Spatial parameters: distance from macroparticle filter (10–20 cm)
- Gas parameters: N<sub>2</sub> flow rate (MFC setting in sccm), working pressure (Pa)
- Vacuum system parameters: cryopump gate valve position, base pressure
- Power supply settings: arc voltage and current, EM-coil voltage and current
- Pulse characteristics: frequency (Hz), pulse width (ms), number of pulses
- QCM frequencies: initial ( $f_0$ ) and final ( $f_1$ ) values for mass determination

Associated oscilloscope waveforms were stored as CSV files for ion current analysis, with filenames linked to the logbook suffix for traceability.

### A.3.2 Ion current data processing

Ion current waveforms were recorded using a Tektronix MSO64 oscilloscope. For each measurement condition, multiple pulses were recorded and processed as follows:

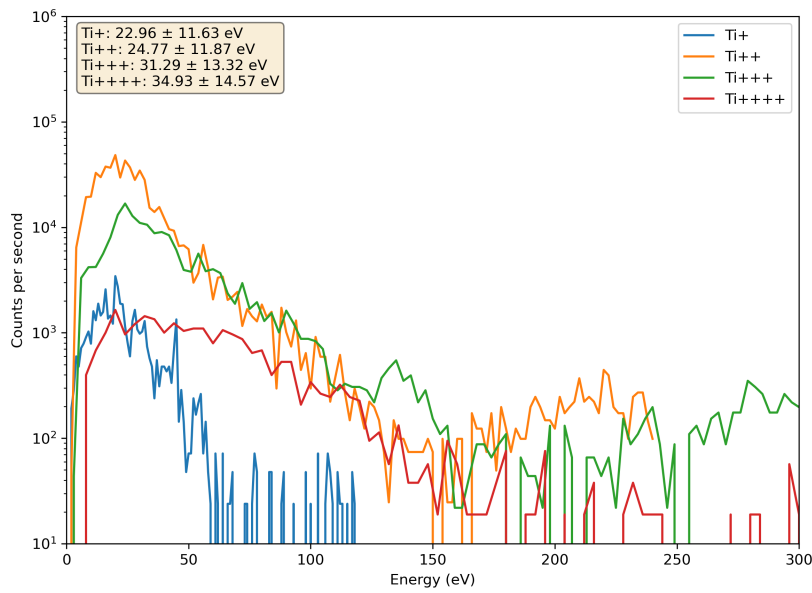


**Figure A.2.** Charge-state-resolved ion energy distribution functions for  $\text{Ti}^+$  through  $\text{Ti}^{4+}$  measured at 14 cm distance with 0.25 T magnetic field and 0.1 Pa  $\text{N}_2$  pressure. Mean kinetic energies and standard deviations are shown in the legend.

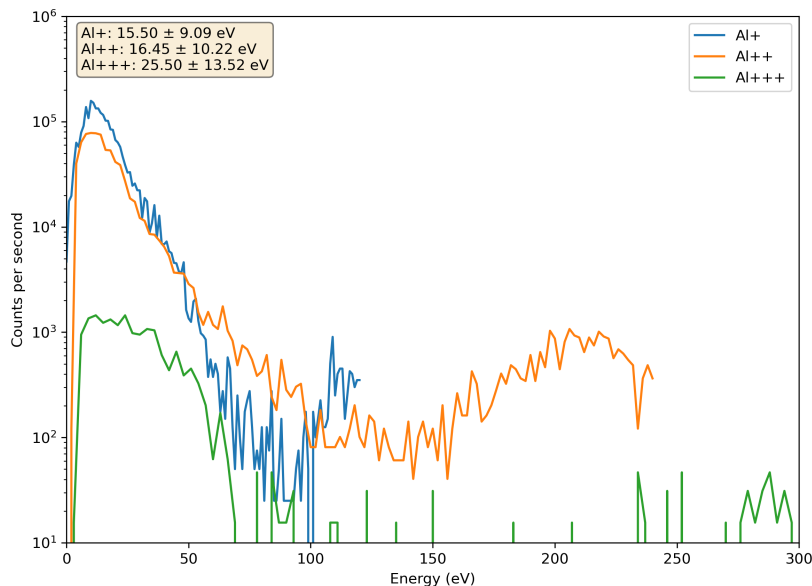


**Figure A.3.** Charge-state-resolved ion energy distribution functions for  $\text{Al}^+$  through  $\text{Al}^{3+}$  measured at 14 cm distance with 0.25 T magnetic field and 0.1 Pa  $\text{N}_2$  pressure. Mean kinetic energies and standard deviations are shown in the legend.

1. **Pulse averaging:** Individual pulse waveforms were averaged to obtain the mean ion current waveform.
2. **Time-integrated current:** The mean ion current over the pulse duration (0–1 ms) was calculated by integrating the averaged waveform and dividing by the pulse width.

The Python script automatically matched logbook entries to oscilloscope CSV files and compiled all parameters into CSV files for analysis.

### A.3.3 QCM data processing

QCM frequency measurements were recorded before and after each set of pulses. The deposited mass was calculated using the Sauerbrey equation (Equation 3.5). The mass deposition rate was obtained by dividing by the number of pulses and the crystal area.

### A.3.4 ERMS data processing

The ERMS data processing was implemented in Python and performed the following operations on the raw spectral data. The underlying measurement principles and correction methodologies are described in Section 3.2.4, while this section focuses on the computational implementation.

1. **Spectral integration:** Raw energy distribution functions (EDFs) for each  $M/Q$  value were averaged over two measurement windows of 20 ms duration each. This averaging improves signal-to-noise ratio while maintaining synchronization with the pulsed arc operation (1 ms pulse duration, 5 Hz repetition rate).
2. **Mass transmission correction:** Correction factors  $T(M/Q)$  were applied to the raw ion signal intensities according to Equation 3.10. The correction function accounts for the mass-dependent detection efficiency of the quadrupole mass filter, which systematically affects lighter ions (Al) differently than heavier ions (Ti). The transmission function was determined through calibration measurements and validated against the known cathode stoichiometry ( $\text{Ti}_{0.75}\text{Al}_{0.25}$ ).
3. **Energy conversion:** The ERMS measures energy-per-charge ( $E/Q$ ) distributions. For multiply charged ions, the measured  $E/Q$  values were multiplied by the charge state  $Q$  to obtain the actual ion energy in eV (Equation 3.9). This conversion was performed for charge states  $Q = 1^+, 2^+, 3^+$  (Al) and  $Q = 1^+, 2^+, 3^+, 4^+$  (Ti).
4. **Statistical extraction:** For each charge-state-resolved energy distribution, the following statistical parameters were calculated:

- Mean ion energy  $\langle E \rangle$  - weighted average over the distribution
- Standard deviation  $\sigma_E$  - characterizing the energy spread
- Peak energy  $E_{\text{peak}}$  - the most probable energy (distribution maximum)

The mean ion energy represents the kinetic energy of ions in that charge state.

5. **Mean charge state calculation:** The mean charge state  $\langle Q \rangle$  for each element was calculated as a weighted average over all detected charge states using Equation 3.21. This parameter is essential for converting the ion current measurements to particle flux (Section 3.4).
6. **Potential energy calculation:** The potential energy  $E_{\text{pot}}$  for each charge state was calculated separately from the cohesive energy and ionization potentials of the cathode material, following Kalanov et al. [6]:

$$E_{\text{pot}}(Q) = E_{\text{coh}} + C \sum_{i=1}^Q E_{\text{ion},i} \quad (\text{A.3})$$

where  $E_{\text{coh}}$  is the cohesive energy (4.85 eV for Ti, 3.39 eV for Al),  $E_{\text{ion},i}$  are the successive ionization energies, and  $C = 0.6$  is a factor accounting for the fraction of ionization energy deposited in the solid. The mean potential energy was then calculated as a weighted average over charge states.

7. **Energy analysis output:** The kinetic energy (measured) and potential energy (calculated) for each element were exported along with their standard deviations. These independent energy components enable investigation of their respective effects on film structure and properties.

The processed results were exported to CSV files containing: pattern identification, mean charge states, mean kinetic energies, mean potential energies, and charge-state-resolved energies for each element. These data were correlated with ion probe and QCM measurements for comprehensive flux and energy analysis. Example charge-state-resolved ion energy distribution functions for titanium and aluminum ions are shown in Figures A.2 and the following figure, measured at 14 cm distance with 0.25 T magnetic field and 0.1 Pa N<sub>2</sub> pressure.

## A.4 Uncertainty analysis

This section documents the uncertainty analysis for measurements reported in this work. Uncertainties were determined from three primary sources: instrument specifications, statistical variations in repeated measurements, and propagation through derived quantities.

### A.4.1 Primary measurements

#### QCM mass measurements

The QCM frequency measurements have a manufacturer-specified resolution that translates to a mass uncertainty of approximately  $\pm 5.64 \times 10^{-10}$  g per measurement. This corresponds to a relative uncertainty of approximately 0.1% for typical deposited masses. This instrumental precision is negligible compared to other uncertainty sources in this work.

The number of pulses (64 in most cases) was controlled digitally and has negligible counting uncertainty. The crystal area ( $1.54 \text{ cm}^2$ ) is specified by the manufacturer.

#### Ion current measurements

Ion current measurements exhibited significant variability due to the non-stationary nature of cathodic arc plasmas. The standard deviation of time-averaged current within individual pulses ranged from 33% to 68% of the mean value (relative uncertainty), with a mean of 45% across all conditions measured.

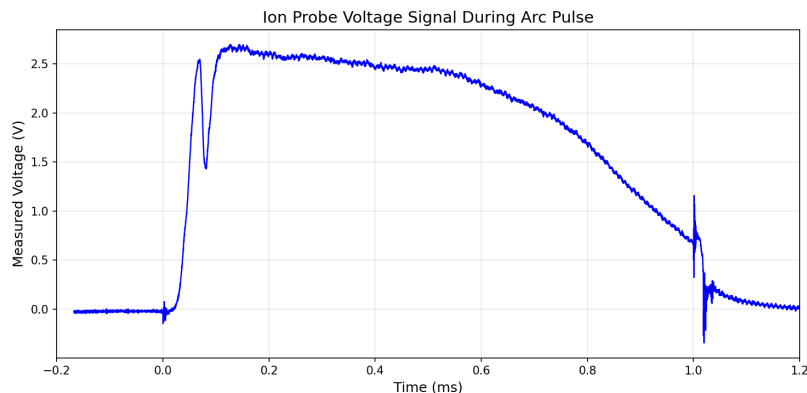


**Figure A.4.** Example ion current waveform showing variability within a pulse. The voltage signal measured across the  $400 \Omega$  resistor is proportional to the ion current. Rapid transients at pulse ignition (0 ms) and termination (1 ms) are excluded from the time-averaged current calculation.

This large variability arises from cathode spot motion and splitting or extinction events, plasma potential fluctuations during pulse ignition and termination, and charge-exchange collisions with background gas that depend on pressure. The oscilloscope (Tektronix MSO64) has a specified voltage measurement accuracy of less than 1%, which is negligible compared to the plasma variability. Error bars on ion current measurements represent the within-pulse standard deviation and characterize the inherent variability of the arc discharge under nominally constant operating conditions.

## ERMS measurements

Mean charge states determined from energy-resolved mass spectrometry (Equation 3.21) have uncertainties ranging from 14% to 24% (relative), with a mean of 20%. This value is calculated as the weighted standard deviation of the charge state distribution:

$$\sigma_Q = \sqrt{\sum_Q w_Q(Q - \langle Q \rangle)^2} \quad (\text{A.4})$$

where  $w_Q = I_Q / \sum I_Q$  are the normalized signal intensities after mass transmission correction. This represents the spread of the charge state distribution and is used in error propagation for flux calculations.

### A.4.2 Derived quantities

Ion flux (calculated from ion current and mean charge state) has significantly larger uncertainties. For ion flux  $\Phi_i = I_{\text{ion}}/(Q \cdot e \cdot A)$ , the relative uncertainty is

$$\frac{\sigma_{\Phi_i}}{\Phi_i} = \sqrt{\left(\frac{\sigma_I}{I}\right)^2 + \left(\frac{\sigma_Q}{Q}\right)^2}, \quad (\text{A.5})$$

where uncertainties were propagated using standard error propagation for uncorrelated variables. This quantity is dominated by the ion current uncertainty (33–68%) and charge state uncertainty (14–24%), resulting in combined uncertainties of 36–72% depending on conditions.

Atomic flux was calculated by converting mass flux to atomic flux using the effective molar mass (determined from film composition measured by ex-situ EDX analysis) and Avogadro’s number. Since composition uncertainties were not formally characterized, the reported atomic flux values do not include propagated uncertainties.

### A.4.3 Uncertainties not quantified

Several systematic uncertainty sources were not explicitly quantified in this work. Spatial plasma uniformity across the measurement area is estimated to contribute less than 10% based on probe size relative to plasma diameter. Long-term calibration drift is expected to be less than 5% as all measurements were completed within 3 months. Temperature effects on QCM sensitivity are minimal since chamber temperature remained stable within  $\pm 2^\circ\text{C}$  and the QCM temperature coefficient is less than 0.1% per degree. Geometric alignment uncertainties in probe positioning of  $\pm 2$  cm correspond to less than 25% flux variation at typical distances.

These effects are expected to be small compared to the dominant uncertainty sources identified above but were not independently characterized.

#### A.4.4 Summary

Table A.1 summarizes the typical uncertainties for key measured and derived quantities. All error bars in figures represent these uncertainties unless otherwise noted. The large uncertainties in ion-based measurements reflect the intrinsic variability of cathodic arc plasmas rather than instrumental limitations.

**Table A.1.** Summary of measurement uncertainties

| Quantity          | Relative Uncertainty | Dominant Source                     |
|-------------------|----------------------|-------------------------------------|
| QCM mass          | 0.01%                | Instrument precision                |
| Ion current       | 33–68%               | Plasma variability                  |
| Mean charge state | 14–24%               | Charge state spread                 |
| Mass flux         | 0.01%                | QCM precision                       |
| Ion flux          | 40–70%               | Ion current + charge state          |
| Atomic flux       | Not reported         | Composition error not characterized |

## A.5 Langmuir probe bias voltage characterization

Before plasma investigations were performed, the functionality of the custom-built ion current probe was verified by characterizing its voltage-current relationship and determining the appropriate operating voltage within the ion saturation regime. This characterization ensures that the probe operates in a regime where the collected current is dominated by ions while effectively repelling electrons.

The bias voltage measurements were conducted without nitrogen in the chamber, at a fixed distance of 10 cm away from the filter, and with an EM-coil strength of 0.25 T.

The relationship between the collected current  $I$  and the bias voltage  $V$  was analyzed using the modified Langmuir equation [15]:

$$I = I_{\text{sat}} \left( 1 - e^{-V/V_0} \right) + m \cdot V \quad (\text{A.6})$$

where  $I_{\text{sat}}$  is the ion saturation current,  $V_0$  is a characteristic voltage, and the linear term  $m \cdot V$  accounts for sheath expansion and collisional effects at higher bias voltages.

Figure A.5 displays the measured ion current as a function of bias voltage. The blue data points represent experimental measurements, while the green curve shows the fit to Equation A.6 and the red dashed line shows the limit between the transition and the saturation regimes of the ion probe.

As the bias voltage increases, the sheath surrounding the probe expands. At higher voltages the sheath becomes non-planar, causing the probe to attract ions from a broader solid angle beyond the immediate frontal area. This geometric effect, combined with ion-neutral collisions within the extended sheath region, produces a residual linear increase in current even in the saturation regime. The linear correction term  $m \cdot V$  in Equation A.6 captures these effects, ensuring accurate modeling across the full voltage range [15, Chap. 7].

The experimental data were fitted using a nonlinear least-squares method in Python, yielding:

$$I_{\text{sat}} = 6.17 \text{ mA}, \quad V_0 = 1.8 \text{ V}, \quad m = 0.023 \text{ mA/V}.$$

The voltage-current characteristic exhibits two distinct regimes:

### 1. Transition Regime (0–70 V):

At lower bias voltages, the probe collects both ions and electrons. As the negative bias increases, electrons are progressively repelled, reducing their contribution to

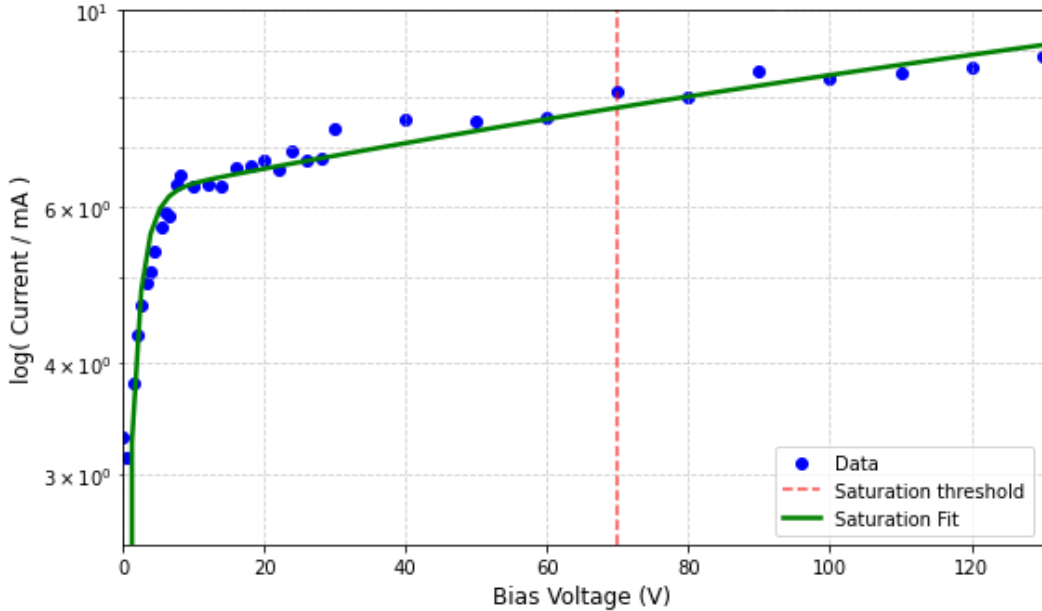


**Figure A.5.** Measured ion current vs. bias voltage, showing fit of eq: A.6. The vertical dashed line at 70 V marks the transition to full ion saturation. Process conditions: no gas, 10 cm from the macroparticle filter, 0.25 T EM-coil strength.

the measured current. This produces a rapid rise in the net ion current as electron repulsion becomes increasingly effective. The exponential term in Equation A.6 dominates this regime, reflecting the transition from mixed electron-ion collection to predominantly ion collection.

## 2. Ion Saturation Regime (70–130 V):

Beyond approximately 70 V, the current curve resembles more a plateau, indicating that the probe has entered the ion saturation regime. At these voltages, the negative bias effectively repels all electrons, and the measured current represents the ion flux to the probe surface. The slight residual increase in current with voltage is captured by the linear term  $m = 0.023 \text{ mA/V}$ , which accounts for sheath expansion and collisional effects as described above.

Based on this characterization, a bias voltage of  $-80 \text{ V}$  was selected for all subsequent plasma measurements. This voltage lies well within the ion saturation regime, ensuring complete electron repulsion.

## A.6 Ion current variation over different pulses

To analyze the pulse-to-pulse variation, approximately 30 single pulses were recorded for each magnetic field strength. The average ion current of each pulse was calculated over the 0–1 ms pulse interval. The final mean and standard deviation were then

determined by combining these averages, allowing for an assessment of the differences between pulses.

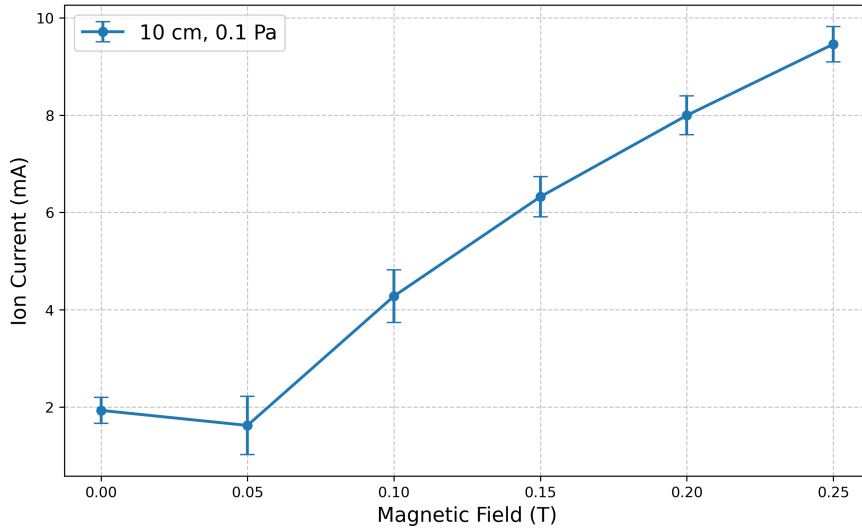


**Figure A.6.** Pulse to pulse variation in mean ion current at varying magnetic fields (0.1 Pa N<sub>2</sub>, 10 cm distance)

| EM-coil field (T) | Mean $I_{\text{ion}}$ (mA) | Std (%) | Range (mA)    | # Pulses |
|-------------------|----------------------------|---------|---------------|----------|
| 0.00              | 1.931                      | 13.8    | [1.13, 2.26]  | 30       |
| 0.05              | 1.622                      | 37.1    | [1.16, 4.85]  | 32       |
| 0.10              | 4.279                      | 12.7    | [2.72, 4.88]  | 31       |
| 0.15              | 6.323                      | 6.6     | [4.99, 6.92]  | 27       |
| 0.20              | 7.996                      | 5.0     | [7.26, 8.78]  | 22       |
| 0.25              | 9.460                      | 3.8     | [8.61, 10.02] | 30       |

**Table A.2.** Summary of pulse measurement statistics for varying magnetic field strengths. Note: The 0.05 T data includes variability from unstable arc behavior at this field strength with a large outlier of 4.85 mA.

In all other measurements, the oscilloscope averaged the voltage signal over multiple pulses to improve signal-to-noise ratio. Therefore, the error reported in subsequent sections primarily reflects variations in ion current within individual pulses, rather than differences between distinct pulses.

## APPENDIX B

---

### Supplementary material

---

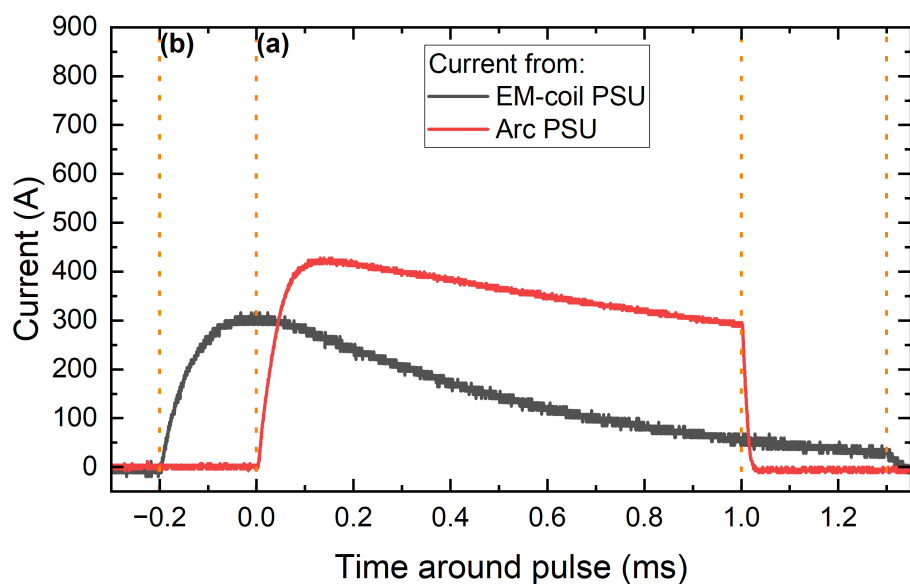


**Figure B.1.** Additional Pulse waveform with the triggering timings (a) and (b) for the Arc-PSU and the EM-coil PSU marked with the orange dashed line for 100V input

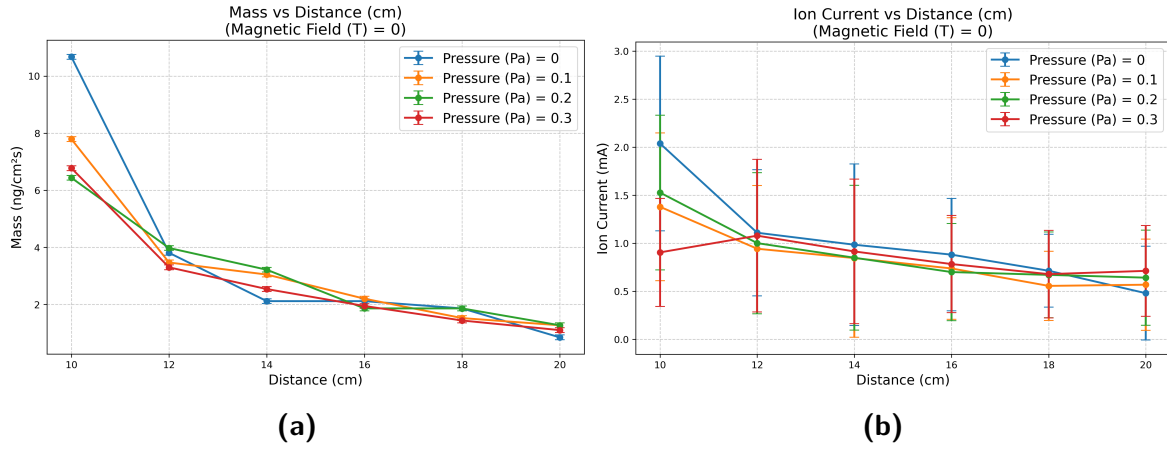


**Figure B.2.** Additional plot for Section 4.1.2. Distance from the filter exit dependence of (a) mass flux and (b) ion current at 0 T magnetic field strength, measured at nitrogen pressures of 0, 0.1, 0.2 and 0.3 Pa

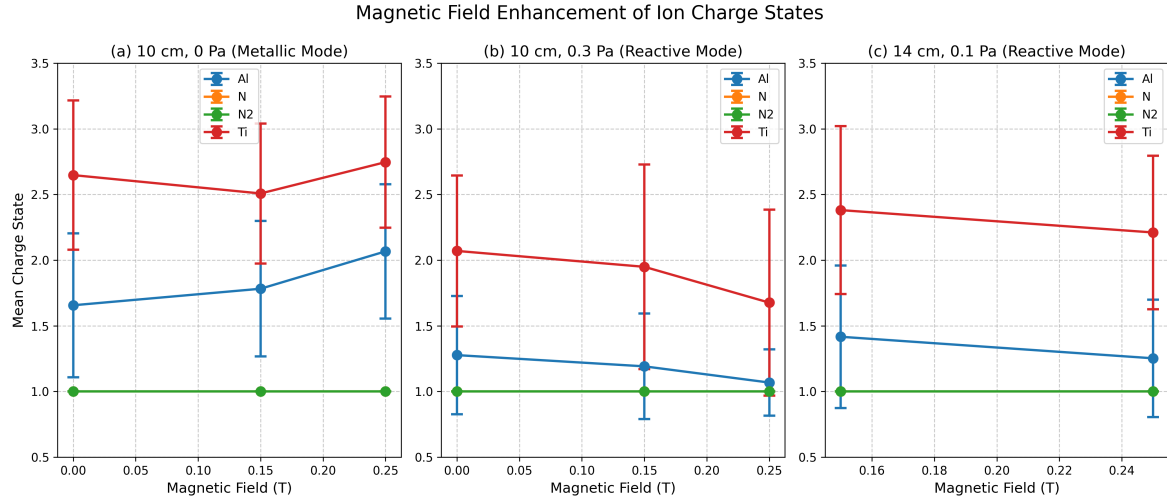


**Figure B.3.** Mean charge state as a function of magnetic field strength for Ti and Al ions under representative conditions: (a) 10 cm distance in metallic mode (0 Pa), (b) 10 cm distance in reactive mode (0.3 Pa), and (c) 14 cm distance in reactive mode (0.1 Pa).

## B.1 Data availability

All raw data files, processed datasets, and analysis scripts are archived and available upon request. The main Python scripts used for data processing include:

- [Ion current and mass csv generator.py](#): Ion current waveform analysis (mean and std) and qcm mass inclusion if provided.
- [Massspec final.py](#): ERMS data integration, mass transmission correction and energy states, mean charge states and potential aswell as kinetic energy extraction.
- [XRD plot stacked.py](#): plotting of stacked XRD plots from .txt files
- [Data sets](#) created and used for the Thesis

**Table B.1.** Complete overview of experimental measurements. All distance/field/pressure combinations not explicitly listed were measured with ion current probe and QCM only. In total: 252 Ion+QCM measurements, 17 ERMS measurements, 4 deposited films

| Distance  | Magnetic Field                   | Pressure                                | Measurements Performed |           |         | Film ID |
|---|----------------------------------|---|------------------------|-----------|---------|---------|
| (cm)  | (T)                              | (Pa)                                    | Ion/QCM                | Mass Spec | Ex-situ |         |
| <i>Systematic parameter scan:</i>               |                                  |   |                        |           |         |         |
| 12, 16, 18                                      | 0, 0.05, 0.1,<br>0.15, 0.2, 0.25 | 0, 0.025, 0.05, 0.075,<br>0.1, 0.2, 0.3 | ✓                      | —         | —       | —       |
| <i>Distance 10 cm — standard conditions:</i>    |                                  |   |                        |           |         |         |
| 10  | 0.05, 0.1,<br>0.2                | all pressures <sup>†</sup>              | ✓                      | —         | —       | —       |
| 10  | 0                                | 0.025, 0.05, 0.075, 0.2                 | ✓                      | —         | —       | —       |
| 10  | 0.15                             | 0.025, 0.05, 0.075, 0.2                 | ✓                      | —         | —       | —       |
| 10  | 0.25                             | 0.025, 0.05, 0.075                      | ✓                      | —         | —       | —       |
| <i>Distance 10 cm — with mass spectrometry:</i> |                                  |   |                        |           |         |         |
| 10  | 0, 0.15                          | 0, 0.1, 0.3                             | ✓                      | ✓         | —       | —       |
| 10  | 0.25                             | 0                                       | ✓                      | ✓         | ✓       | 003     |
| 10  | 0.25                             | 0.1                                     | ✓                      | ✓         | ✓       | 004     |
| 10  | 0.25                             | 0.2                                     | ✓                      | ✓         | —       | —       |
| 10  | 0.25                             | 0.3                                     | ✓                      | ✓         | ✓       | 002     |
| <i>Distance 14 cm — standard conditions:</i>    |                                  |   |                        |           |         |         |
| 14  | 0, 0.05, 0.1, 0.2                | all pressures <sup>†</sup>              | ✓                      | —         | —       | —       |
| 14  | 0.15                             | 0, 0.025, 0.05,<br>0.075, 0.2, 0.3      | ✓                      | —         | —       | —       |
| 14  | 0.25                             | 0.025, 0.05, 0.075, 0.2                 | ✓                      | —         | —       | —       |
| <i>Distance 14 cm — with mass spectrometry:</i> |                                  |   |                        |           |         |         |
| 14  | 0.15                             | 0.1                                     | ✓                      | ✓         | —       | —       |
| 14  | 0.25                             | 0                                       | ✓                      | ✓         | ✓       | 008/010 |
| 14  | 0.25                             | 0.1                                     | ✓                      | ✓         | ✓       | 011/013 |
| 14  | 0.25                             | 0.2                                     | ✓                      | ✓         | ✓       | 014     |
| 14  | 0.25                             | 0.3                                     | ✓                      | ✓         | ✓       | 009/011 |
| <i>Distance 20 cm — standard conditions:</i>    |                                  |   |                        |           |         |         |
| 20  | 0, 0.05, 0.1,<br>0.15, 0.2       | all pressures <sup>†</sup>              | ✓                      | —         | —       | —       |
| 20  | 0.25                             | 0.025, 0.05, 0.075, 0.1, 0.2            | ✓                      | —         | —       | —       |
| <i>Distance 20 cm — with mass spectrometry:</i> |                                  |   |                        |           |         |         |
| 20  | 0.25                             | 0, 0.3                                  | ✓                      | ✓         | —       | —       |

<sup>†</sup>all pressures = 0, 0.025, 0.05, 0.075, 0.1, 0.2, 0.3 Pa

Ion/QCM: Ion current probe and quartz crystal microbalance measured at the same time

Mass Spec: Energy-resolved mass spectrometry (ERMS)

Ex-situ: XRD, SEM, EDX, profilometry characterization of deposited films